NTNU
Norwegian University of
Science and Technology

Metabolic Profiling of Prostate Cancer Tissue Using Magnetic Resonance Spectroscopy

An investigation into prostate heterogeneity
and cancer characteristics in a transgenic
mouse model, with a comparison to human
disease

Silje Løveng

Silje Løveng

Metabolic Profiling of Prostate Cancer Tissue Using Magnetic Resonance Spectroscopy

An investigation into prostate heterogeneity and cancer characteristics in a transgenic mouse model, with a comparison to human disease

Master thesis
for the degree of Master of Science

Trondheim, June 2017

Norwegian University of Science and Technology
Faculty of Natural Sciences and Technology
Department of Physics

NTNU
Innovation and Creativity

Abstract

Using ^{1}H High-Resolution Magic Angle Spinning Magnetic Resonance Spectroscopy, tissue samples of both healthy mouse prostate and different grades of mouse prostate cancer in a transgenic mouse model were analysed to investigate which metabolites are present at different stages of mouse prostate cancer. The trends in the metabolic changes were compared to human prostate cancer, and found to be of similar nature, with elevation of lactate, alanine, creatine, taurine and glycine, and decreased levels of citrate, glycerophosphocholine, phosphocholine and choline.

Differences in the metabolism of the four distinct lobes of the mouse prostate were also investigated, and large variations between the lobes were identified. The ventral prostate of mice seems to be the one that mimics human prostate cancer the best, despite being claimed to have no human counterpart based in previous histology. The large differences between the lobes imply that great care should be taken when measuring metabolite levels, as inconsistencies could lead to misinterpreting results.

Future work should include histopathology to secure proper classifications of the mouse prostate cancer, and comparison with human disease could be improved by performing absolute quantification and including more metabolites.

Sammendrag

Vevsprøver av både frisk museprostata og ulike grader av prostatakreft i mus ble analysert ved hjelp av ^{1}H høyoppløselig magisk vinkelspinning magnetisk resonans spektroskopi for å undersøke hvilke metabolitter som er tilstede ved ulike grader av kreft. Endringer i metabolittkonsentrasjoner fra frisk prostata til de mest aggressive tumorene ble sammenlignet med tilsvarende funn fra prostatakreft hos menn, som viste seg å være av samme karakter. Disse felles-trekkene innebar forhøyede verdier av laktat, alanin, creatine, taurin og glysin, og lavere verdier for sitrat, glyserofosfokolin, fosfokolin og kolin.

Forskjeller mellom metabolismen til de fire ulike prostatalappene hos mus ble også undersøkt, og store ulikheter mellom lappene ble oppdaget. De ventrale prostatalappene hos mus ser ut til å være de som ligner utviklingen av prostatakreft hos mennesker best, til tross for at denne prostatalappen er ansett som den eneste uten en menneskelig motpart basert på tidligere histologiske sammenligninger. De store variasjonene i metabolittkonsentrasjoner innebærer at man må være svært nøye når metabolittnivåene skal måles for å unngå feiltolkning av resultater.

Fremtidig arbeid bør innebære histopatologi for å forsikre seg om at vevsprøvene fra musene med prostatakreft er korrekt klassifisert. I tillegg vil absolutt kvantifisering av metabolittkonsentrasjoner, samt å inkludere flere metabolitter i analysen, forbedre og forenkle sammenligningen med prostatakreft hos menn.
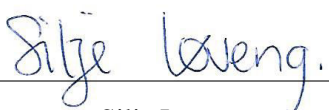
Preface

The work associated with this thesis has been conducted at the MR Cancer Group, Department of Circulation and Medical Imaging, Faculty of Medicine and Health Sciences, NTNU, Trondheim. This project is a continuation of the work with my project thesis the previous semester.

My supervisor at the MR Cancer Group was Dr. Deborah Katherine Hill, and to her I direct a special gratitude. Her engagement, guidance and support through this last year have been of great help as well as a strong motivating force. Her enthusiasm sure is contagious!

I would also like to thank everyone at MR Cancer Group that have offered their assistance. Especially thanks to Dr. Trygve Andreassen for both showing me how to perform HR-MAS MRS and how to use Chenomx, as well as providing me with some help with PCA. Thanks to Dr. Leslie Euceda Wood for teaching me how to preprocess and analyse spectra, and to Dr. Tonje Husby Haukaas for showing me sample preparation. I also thank Prof. Tone Frost Bathen for giving me the opportunity to work with this amazing group, and for her and Dr. May-Britt Tessem's guidance during the completion of the thesis. I have really enjoyed my time at MRCG!

At last, a thanks to my nearest and dearest is in order. To my family, for their support that has been invaluable during these five years in Trondheim, especially when the road ahead seemed long and insurmountable. And to my dearest Thomas, for always being there for me, cheering me on. Thank you for sharing your life with me!

Silje Løveng

Contents

List of Tables

List of Figures

Abbreviations

ALS Asymmetric Least Squares. 19, 28

AP Anterior Prostate. 4, 5, 31, 32

ATP Adenosine Triphosphate. 8

CPMG Carr-Purcell-Meiboom-Gill. 17, 18, 26–28

DLP Dorsolateral Prostate. 4, 5

DP Dorsal Prostate. 4, 31–33

FID Free Induction Decay. 15, 17, 27

GPC Glycerophosphocholine. 10

GU Genitourinary. 30

HES Haemotoxylin Eosin Saffron. 29

HR-MAS High Resolution Magic Angle Spinning. 2, 16, 18, 23–27

JRES J-resolved. 18, 19, 26, 27

LP Lateral Prostate. 4

MRS Magnetic Resonance Spectroscopy. 2, 11, 12, 16, 18, 23–27

MVA Multivariate Analysis. 20, 21

NMR Nuclear Magnetic Resonance. 20

NOE Nuclear Overhauser Effect. 17

NOESY Nuclear Overhauser Effect Spectroscopy. 17, 18, 26, 27

OAA Oxaloacetate. 8

PC Principal Component. 21, 34, 35

PCA Principal Component Analysis. 2, 21, 29, 31, 34, 35

PCa Prostate Cancer. 1, 2, 6, 7, 10, 11, 30

PD Poorly Differentiated. 7, 11, 24, 29–33, 35

PIN Prostatic Intraepithelial Neoplasia. 7, 11

ppm parts per million. 16, 28, 29, 35

PQN Probabilistic Quotient Normalisation. 20, 29

PSA Prosate-Specific Antigen. 1, 7

PtdCho Phosphatidylcholine. 9, 10

RF Radio Frequency. 11, 13, 14

ROI Region of Interest. 28, 29

SE Spin-Echo. 15, 17

TCA Tricarboxylic Acid. 8–10

TRAMP Transgenic Adenocarcinoma of the Mouse Prostate. 1, 2, 11, 23, 24, 29, 30, 34, 35

VP Ventral Prostate. 1, 4, 5, 11, 24, 30, 31, 33, 34

WD Well Differentiated. 7, 11, 24, 29–33, 35

1 | Introduction

Prostate Cancer (PCa) is the most frequently diagnosed cancer among men in developed countries, and it is the second leading cause of cancer deaths among the same male population(1). Great improvements to both diagnostics, such as Prosate-Specific Antigen (PSA) screening(2, 3), and treatments have been seen in the last years, which have consequently reduced disease mortality(1). The more extensive screening of PCa and increased rate of diagnosis(1) have also led to overdiagnoses(4), with subsequent overtreatment and increased incidence of side effects depending on treatment method, involving urinary incontinence, erectile dysfunction and bowel problems(5). The aggressiveness of human PCa varies between the patients, and the aggressiveness will determine if and how the disease will be treated; more reliable diagnostic and monitoring tools will facilitate personalised treatment options for patients after diagnosis. Further improvement in the field of PCa is therefore needed, and clinically relevant and reliable models of the disease are important tools in order to achieve this.

Studies of PCa are performed both in vitro on cell cultures(6) and in vivo with animals. Mice are often used in this research, and the models are either made by transplantation of PCa cells(7, 8) or they are genetically engineered to develop PCa(9). The TRAMP model was the first genetically engineered mouse model of PCa(9), and is widely used. The model holds similar traits to the morphological progression of human PCa, and with the rapid development of cancer in 100% of the mice, TRAMP mice form an effective and solid platform for studies of the disease.

1.1 Related work

Little work has been done in order to investigate the metabolic characteristics of PCa in TRAMP mice, furthermore, the metabolic profiles of the different lobes of the mouse prostate have not been investigated. Previous projects have studied the citrate concentrations in the Ventral Prostate (VP) of TRAMP mice(10), and in-

vestigated the metabolic features of the TRAMP prostate using tissue samples that were randomly chosen among the four different prostate lobes of each mouse(11).

In an introductory project(12), the metabolic profile of 14 prostate cancer tissue samples from TRAMP mice were compared to a prostate tissue sample from a c57 mice that served as a healthy control. Indications of altered metabolism in the different grades of PCa in TRAMP mice were found, as well as indications of differences in the metabolism of the mouse prostate lobes. This project is a continuation of this, comprising more samples and more extensive analysis.

1.2   Approach and aim of the project

The aim of this project is to further investigate if and how the TRAMP model resembles human disease in order to add knowledge to the already existing literature on the TRAMP model. Further, the heterogeneity of the mouse prostate lobes from both healthy and TRAMP mice will be looked into.

[1]H HR-MAS Magnetic Resonance Spectroscopy (MRS) is the chosen laboratory technique. This method provides the desired information about the metabolic profiles while it enables following histology/histopathology of the exact same tissue samples, thus increasing the amount of information these mouse tissue samples will provide. In the continuation of the work with this project, these two techniques combined offers great potential of a solid understanding of the mouse prostate in both healthy and diseased mice, and histology of the samples is planned after the completion of this thesis.

Principal Component Analysis (PCA) will be used to look for clustering or trends within the data. PCA is exploratory in nature, and will identify patterns within the data without any prior information. Based on findings in the PCA, clusters of data points can be identified. Clustering occurs because the data points share similar metabolic signatures in some important metabolites. The metabolites are identified using a loadings plot, and can be quantified through integration, yielding the relative concentrations of the metabolites in the four lobes of the mouse prostate within the different cancer classifications and healthy controls.

The findings from this project will determine whether the TRAMP model is metabolically similar to human disease. This could have major implications in the recommendations for the use of this model for future studies, such as preclinical tests of new PCa drugs. This study is the first to investigate metabolic profiles of the different lobes of the mouse prostate, and the findings will be important to any future urological research employing mouse models.

1.3 Outline

The thesis is organised into the following chapters:

Background   Relevant background material for the experiments and analysis is presented in this chapter.

Methods   In this chapter, the methods used all the way from the harvesting of samples to the analysis of the data sets are described.

Results   The results from the analysis are presented through figures.

Discussion   Interpretation of the results and the consequences of these are presented along with future plans.

Conclusion   A summarising outlook of the findings.

2 | Background

The following section provides the necessary background for this project, without delving too deep into the topics, but enough to sufficiently justify the chosen methods. Where appropriate, the literature is referenced for a more detailed description of the background theory. Parts of the following chapter contains adapted material from the initial project(12), revised to reflect the project continuation.

2.1 The prostate

2.1.1 Human prostate

The prostate is part of the male reproductive system, and the human prostate is located between rectum and the penis, right below the bladder. It surrounds the the urethra, and is often described as walnut-sized. The main function of this gland is to secrete an alkaline fluid which contributes to the seminal fluid. This prostatic secretion protects the genetic material in the semen, in addition to increasing both the mobility and survival of the sperm cells.

Fig. 2.1 **A)** shows the anatomy of the human prostate, which is divided into four glandular regions based on their individual histology(13). These are called the peripheral zone, the central zone, the transition zone and the anterior fibromuscular stroma.

2.1.2 Mouse prostate

The mouse prostate is located in a similar position to the human prostate, but unlike the human prostate, the mouse prostate consists of four distinct lobes, as shown in fig. 2.1 **B)**. These anatomical structures are named after their spatial orientation; the Anterior Prostate (AP), the Dorsal Prostate (DP), the Lateral Prostate (LP) and the VP. The DP and LP are often referred to as one; the dorsolateral prostate(14). Analysis of the gene expressions of the Dorsolateral Prostate (DLP) and the two

other lobes indicates that the DLP is analogous to the peripheral zone of the human prostate(15), despite some differences in histology(14). The AP is considered as the mouse counterpart to the central zone of human prostate, while the VP lacks any human counterpart.
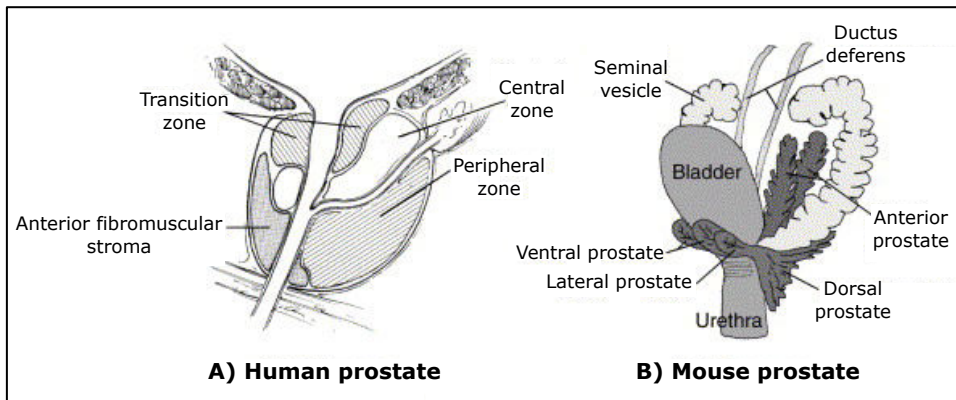
Figure 2.1: Illustration of **A)** human prostate and **B)** mouse prostate. The figure was adapted from (16) with permission.

2.2   Cancer

Cancer is a collective term which include all diseases caused by cells that uncontrollably proliferate. This results from defects in regulatory circuits of the cells, which in normal cells prohibit such a high proliferation rate.

There are several characteristics which together form the basis for how the development of cancerous cells are possible, as described by Hanahan and Weinberg(17, 18), and fig. 2.2 sums up the ten hallmarks that are common for all types of cancer. Through genetic alterations, cells that possess these characteristics have evolved mechanisms that enable them to avoid normal cell regulation. These mechanisms include upregulation of receptors for growth factors, as is the case for the hallmark of sustained proliferative signaling. Evading growth suppressors will further aid the proliferation of cancerous cells, as tumour suppressors are designed to hinder fast cell proliferation. In combination with rest of the hallmarks, these traits enable cancer cells to maintain their growth and to evade programmed cell death, leading to tumour survival.

Cancer cells are less differentiated than normal cells(19), and in combination with the fast cell growth and avoidance of cell death, cancer cells will invade and destroy surrounding tissues. Invasion can occur via blood vessels and lymph channels,

which facilitates the spread of cancer throughout the body, potentially resulting in metastases at other sites.

Figure 2.2: An overview of the ten hallmarks of cancer which form the basis for all cancers. Illustration from Løveng(12), adapted from Hanahan and Weinberg(17) with permission.

Tumours and cancers are not always the same, but some tumours are cancerous. Benign tumours are non-cancerous, meaning that they are the results of abnormal cell growth, but they are not capable of spreading. Malignant tumours are cancerous and will invade surrounding areas as well as spreading to other sites in the body, and this spread is referred to as metastasis. Several grading systems exist both for benign and malignant tumours, and their role is to indicate how differentiated the tumour is compared to that of the original tissue. The less differentiated the cancer is, the more aggressive will it be. This classification is based on histopathology, and in cancers these classifications help guide the treatment as well as being used to predict the prognosis for each patient.

2.2.1 Prostate cancer

Human PCa is cancer that evolves in the prostate gland, and is the most frequently diagnosed cancer among men in the western world, and the second most common

reason for male cancer deaths(1). In Norway, close to 5000 new cases were diagnosed in 2015, but when comparing 5 year survival, PCa was the third least deadly cancer(20).

The majority of the PCa arise in the peripheral zone, a little more than 20% arise in the transition zone, and less than 10% arise in the central zone(21). Cancer in the transition zone is linked to better prognoses than cancer in the peripheral zone(22). Cancer in the anterior fibromuscular stroma seems to be originating from the transition zone(23).

The progression of PCa is associated with Prostatic Intraepithelial Neoplasia (PIN) as the preinvasive stage(24), before it develops into Well Differentiated (WD) and then Poorly Differentiated (PD) cancer, with metastasis to bone, lungs and liver, among other(25).

A reason for the numerous diagnoses is more widespread use of screening processes due to improved diagnostic tools, such as PSA testing. These tests has led to earlier detection of PCa, but elevated PSA levels can also be associated with benign tumours. Misdiagnoses and overtreatment of PCa are therefore a consequence of the increased number of tests performed, and further development of diagnostic tools for both detecting the disease as well classify the aggressiveness of the cancer is therefore needed. Many different potential biomarkers of PCa have been proposed, such as citrate and spermine(26), lactate and alanine(27) and different proteins(28). All of these propose more accurate diagnosis, better monitoring of PCa progression, and improved customisation of treatments.

2.3   Cell cycle and changes in metabolism

Among the hallmarks of cancer is the alteration of the metabolism(18, 17). As cancer cells proliferate at a much higher speed than normal cells, their need for both energy and building blocks to produce new cells is much higher in cancerous tissue than what is required in normal tissue. The alterations are though quite complex and far from fully understood, so further analysis of the mechanisms in tumours compared to healthy tissue is much needed.

Regardless of how well understood the cell cycle and metabolic mechanisms are, alterations can be detected through analysis of the metabolite concentrations at a defined location. The metabolites that are detected will say something about which processes are conducted within the tissue, as they are linked to different pathways as intermediates or products.

2.3.1 Glycolysis

Glycolysis is the biochemical pathway in which the 5 carbon compound glucose is converted into the three carbon compound pyruvate. This is done through a series of ten steps, where the net yield of energy is two Adenosine Triphosphate (ATP) molecules per molecule of glucose(29). Fig. 2.3 illustrates briefly how two pyruvate molecules is made from a glucose molecule, and the three options for further reactions. In some mammalian cells and tissues, the glycolytic pathway is the sole source of metabolic energy, sperm being one of these.
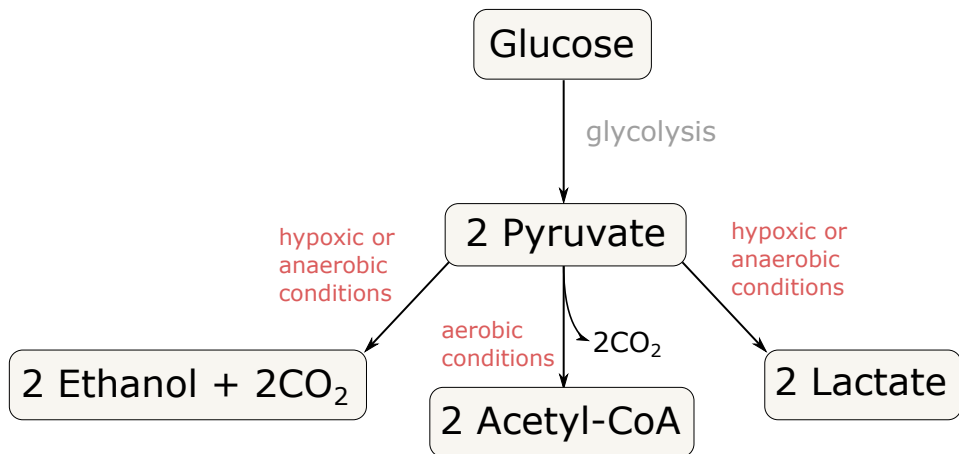
Figure 2.3: Overview of how a glucose molecule is oxidised into 2 pyruvate molecules through glycolysis. Depending on the conditions, these two molecules can be further oxidised to yield more energy.

2.3.2 The Tricarboxylic acid cycle

The Tricarboxylic Acid (TCA) cycle, also called the citric acid cycle or Krebs cycle, is the enzyme driven cyclic process in which acetyl-CoA made from pyruvate condenses with Oxaloacetate (OAA) to form citrate, which then is oxidised into two CO_2 molecules in addition to the energy carrier GTP and fuel ($NADH/FADH_2$) for the electron transport chain which further generates ATP(29). An illustration of the cycle is shown in fig. 2.4. The intermediates of the TCA cycle are also needed in other pathways of cells, and some of the produced intermediates are therefore removed from the cycle. Succinyl-CoA for instance, is required for producing e.g. cytochromes and chlorofyll, while α-ketoglutarate and oxaloacetate are both precursors for many amino acids.
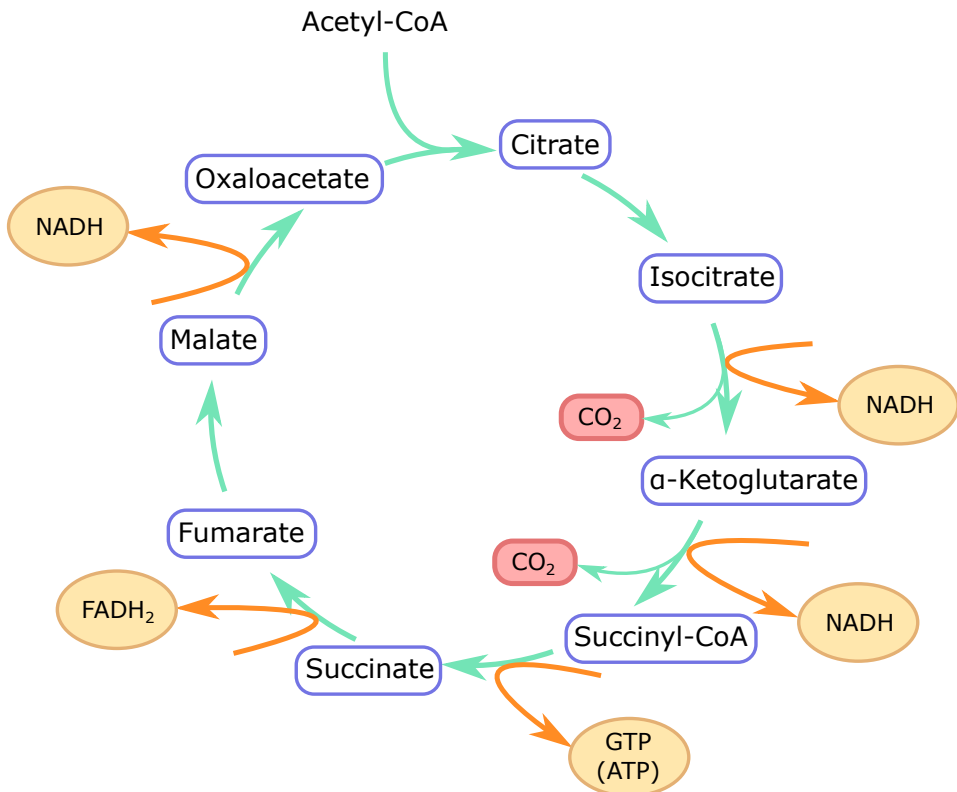
Figure 2.4: Overview of intermediates and product of the TCA cycle. Two CO_2 molecules along with energy carriers are produced before the cycle starts over again.

2.3.3   Choline phospholipid synthesis

The choline phospholipid synthesis is one of two branches of the Kennedy pathway(30), in which Phosphatidylcholine (PtdCho) is produced *de novo* from choline, with phosphocholine as an intermediate. Fig. 2.5 gives an overview of the pathway. PtdCho is among the main components of the membranes in mammalian cells(29), and the building of new cells will therefore require production of this compound. The steps in this process is enzyme driven.
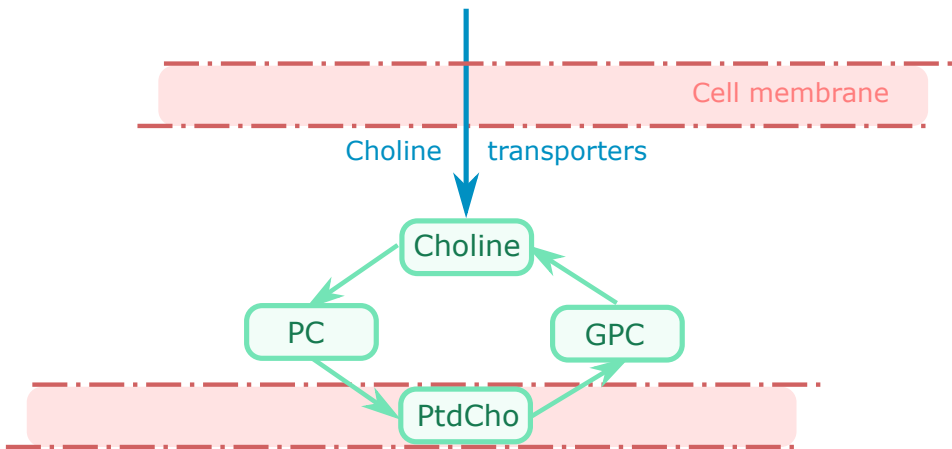
Figure 2.5: One of the two branches of the Kennedy pathway, where phosphatidylcholine (PtdCho) is synthesised from choline. The process is reversible.

2.3.4 Important metabolites associated with prostate cancer

As cancer cells behave differently to normal cells, their requirements to thrive are also different. The high proliferation in cancerous tissue leads to an increased need of energy and building blocks, and the environment within the prostate will therefore be altered.

Citrate is found in high levels in normal prostate, as it is a main component of the prostatic fluid(31), and since citrate is a product in itself in the prostate, the TCA cycle is not utilised as an energy source(32). The increased need of energy in PCa will exploit the great energy yield of the TCA cycle, and the citrate concentration within the prostate will decrease as a result of this altered metabolism. Reduced levels of citrate is therefore linked to PCa(33).

The high proliferation rate will demand more PtdCho to build cell membranes. Increased expression of choline transporters is therefore detected in PCa(34), which will lead to identification of higher choline and phosphocholine concentrations(35). As Glycerophosphocholine (GPC) is a product of the breakdown of PtdCho, it says something about the turnover of the phospholipid synthesis, and is also found to be elevated in PCa(36).

Increased levels of lactate is also linked to PCa(27), partly because of hypoxic environments within tumours which will lead to anaerobic fermentation of glucose as illustrated in fig. 2.3, but also due to the Warburg effect, implying that cancer cells choose a less favourable energy pathway in order to keep more carbon atoms to produce building blocks(37).

Changes in the concentrations of other metabolites related to these syntheses directly or indirectly are also found, including polyamines, alanine, glutamate, glutamine, succinate(36, 38).

2.4 Mouse models of prostate cancer - The TRAMP model

Animal models of PCa are extremely helpful tools for studying the disease, diagnostic tools and treatments, but modelling PCa in mice is difficult. A reason for this is that mice do not usually develop PCa spontaneously(39) as humans do. Genetically engineered mouse models are have therefore been developed(9), with the TRAMP(40) model being one of the most widely used(41). It has proven to be a versatile model for PCa, with similar traits as the progression of human PCa which develops from well differentiated to poorly differentiated, and with metastasis to other sites(42).

The model is based on the wild-type laboratory mouse model C57BL/6 (c57), and was developed using the prostate steroid binding protein C3-1 and Simian virus 40 (SV40) early region. C3-1. However, it is not specific to the prostate, so probasin minimal promoter was fused to SV40 early region and resulted in variable expression. Selecting the lines with higher transgene expression in ventral and dorsal lobes lead to the TRAMP model(40).

The model shows prostatic disease with a frequency of 100%, and in combination with rapid progression, the TRAMP model offers an effective and reliable model of PCa. The origin of cancer in the prostate of the TRAMP model is commonly found in the dorsolateral prostate, which is resembling the peripheral zone of the human prostate where the majority of human PCa origins.

A newer trait of the TRAMP mice that has been discovered, is the indications of subtypes within the TRAMP model(43). This is based on the differences in the progression of the disease in the model that leads to either WD and to PD PCa. The PD tumours seems to be developed spontanously at early age in the VP(43, 44) and without any early PIN detection, suggesting that the mechanisms behind the WD and PD PCas are different. The suggested subtype involves the mice who develop fast-growing neuroendocrine carcinoma, usually originating in the VP(43).

2.5 Magnetic resonance spectroscopy

The phenomenon which forms the basis of MRS is that the nuclei have a spin, or a magnetic moment, that will align with an external magnetic field, and these spins will absorb and emit Radio Frequency (RF) pulses. This phenomenon were first

described by Bloch(45) and Purcell(46) already in 1936, and MR has since then evolved into an important tool within many different fields. MRS can be used to identify the different compounds in a sample, as well as to determine the molecular structure of the sample.

The nuclei needs an odd number of protons or neutrons to have a spin that can be observed with MR, and nuclei like ^{1}H, ^{13}C and ^{31}P are commonly studied(47). If the nuclei have an even number of both protons and neutrons, their spins will even each other out, causing the total spin of the nuclei to be zero.

The intrinsic spin $s = \frac{1}{2}$ for the proton(48), allowing two possible states $m_s = \pm\frac{1}{2}$. The magnetic moment $\boldsymbol{\mu}$ defines the energy shift ΔE experienced within an external magnetic field $\mathbf{B}$ by $\Delta E = -\boldsymbol{\mu}_s \cdot \mathbf{B}$ with the magnetic moment

$$\boldsymbol{\mu}_s = g_S \frac{e}{2m_p}\mathbf{S}, \tag{2.1}$$

where $\mathbf{S}$ is the the spin vector $\mathbf{S} = (S_x, S_y, S_z)$, $g_S \approx 2$ is the g-factor of the system, e is the proton charge and m_p is the proton mass.

For general systems,

$$\boldsymbol{\mu}_s = \gamma\mathbf{S}, \tag{2.2}$$

where γ is the *gyromagnetic factor* of the system.

The spins will be randomly distributed, but when an external magnetic field is applied the spins will align either parallel or antiparallel to the field. For a spin-$\frac{1}{2}$ particle, this corresponds to a splitting of the energy levels into one lower energy parallel spin state and one higher energy antiparallel spin state. This splitting of energy levels is known as the Zeeman effect(49). The spins will oscillate between the two states with a statistical bias towards the energetically favourable parallel state given by the Boltzmann factor

$$\frac{F(\text{parallel})}{F(\text{antiparallel})} = \exp\left\{-\frac{\Delta E}{k_B T}\right\}, \tag{2.3}$$

where F is the population function, k_B is the Boltzmann constant and T is the temperature. This results in a net ensemble magnetisation $\vec{M} \neq \vec{0}$. With increasing external magnetic flux density $|\mathbf{B}|$, the energy splitting between the states caused by the Zeeman effect also increases, such that more nuclei will be in the parallel spin state at thermal equilibrium. From $\Delta E = -\boldsymbol{\mu}_s \cdot \mathbf{B}$, this causes the system magnetisation $|\vec{M}|$ to increase proportionally to the external magnetic field.

Under the influence of an external magnetic field $\mathbf{B} = (0, 0, B_0)$ directed along the z-axis, the spin precesses in the xy-plane with a characteristic frequency, known as the Larmor-frequency(48).

This can be seen by calculating the time-evolution of the spin operator, $\hat{\mathbf{S}} = (\hat{S}_x, \hat{S}_y, \hat{S}_z)$

$$\frac{d}{dt}\langle\hat{\mathbf{S}}\rangle = -i\hbar \left\langle [\hat{H}, \hat{\mathbf{S}}] \right\rangle + \left\langle \frac{d\hat{\mathbf{S}}}{dt} \cdot \right\rangle. \tag{2.4}$$

Here,

$$\hat{H} = -\hat{\boldsymbol{\mu}}_s \cdot \mathbf{B} = -\gamma B_0 \hat{S}_z = -\omega \hat{S}_z, \tag{2.5}$$

where ω is the Larmor frequency. Using the commutator rules for angular momentum operators,

$$\frac{d}{dt}\langle S_x \rangle = -\omega \langle S_y \rangle, \quad \frac{d}{dt}\langle S_y \rangle = \omega \langle S_x \rangle, \quad \frac{d}{dt}\langle S_z \rangle = 0. \tag{2.6}$$

These equations describe a projection in the xy-plane rotating with an angular frequency ω_0,

$$\langle S_x \rangle(t) = A \, \Re \, e^{i(\omega t + \phi)} \quad \langle S_y \rangle(t) = A \, \Im \, e^{i(\omega t + \phi)}, \tag{2.7}$$

where A is the magnitude and ϕ is the phase offset. Unlike the $\vec{M}_z$-component, $\vec{M}_{xy} = \vec{0}$ under influence of an external field because phase decoherence between the randomly distributed phases of spins in this plane causes the magnetisation in the plane to average to 0.

After the spins have aligned along the external magnetic field, RF pulses at the Larmor frequency $\omega = \gamma B_0$ are aimed at the sample, exciting the system to higher energy states by forcing an increased amount of antiparallel spins. The absorbed waves also induces phase coherence in the xy-plane, which yields a net ensemble magnetisation $\vec{M}_{xy} \neq \vec{0}$. In other words, these effects combined causes the precessional motion of the net ensemble magnetisation to partially or fully collapse onto the xy-plane given a RF energy density. The Larmor precession and the transition that occurs during excitation is illustrated in fig. 2.6.
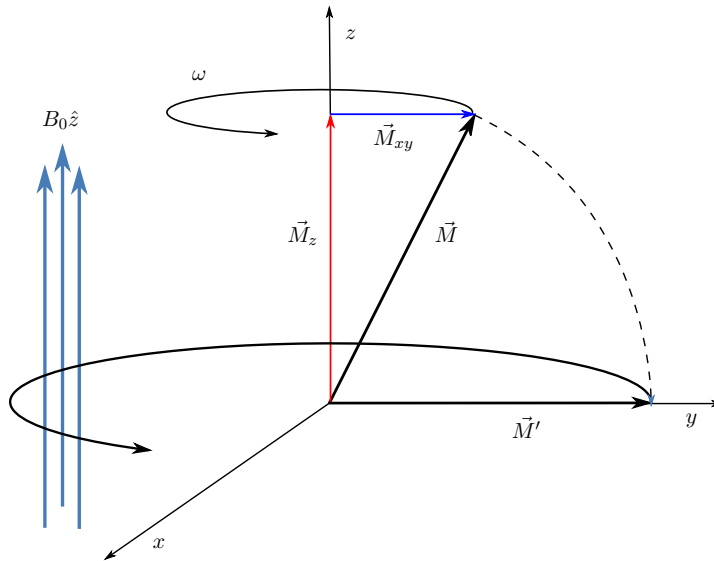
Figure 2.6: Illustration of the net magnetisation of an ensemble of spin-$\frac{1}{2}$ particles suspended in a magnetic field $B_0\hat{z}$. The magnetisation precesses around the z-axis, and applying an increasingly strong RF signal causes the magnetisation to gradually collapse onto the xy-plane from reduced parallel/antiparallel spin ratio and increased phase coherence in the Larmor precession of the individual spins.

After the RF signal has ceased, the magnetisation vector continues to have a rotating projection in the xy-plane. This rotating component produces RF-radiation at the excitation frequency. This emission reduces the energy of the system, more spins align in the lower energy parallel state and the M_z magnetisation gradually returns to its normal state in a process known as T_1-relaxation.

In this process, the magnetisation in z-direction recovers in an exponential way,

$$\vec{M}_z(t) = |\vec{M}| \left(1 - \exp\left\{ -\frac{t}{T_1} \right\} \right) \hat{z}, \tag{2.8}$$

where T_1 is the characterising relaxation constant for different types of tissue, and is defined as the time at which e^{-1} of the excess fraction of antiparallel states due to the RF-signal has returned to parallel. Some of the energy is also lost to heating up surrounding lattice.

Another effect of removing the RF source is dephasing of the spins so that the magnetisation smears in the xy-plane, causing a reduction in the signal over time. This happens because of random spin-spin-interactions between a particle and its neighbours, temporarily modifying the local magnetic field around a single nucleon.

This shifts the Larmor-frequency of the nucleon in relation to the natural Larmor-frequency induced by the external magnetic field. Consequently, global spin decorrelation and signal decay occurs. This dephasing is known as T_2-relaxation, and follows an exponential decay curve,

$$\vec{M}_{xy}(t) = |\vec{M}| \exp\left\{-\frac{t}{T_2}\right\} [\Re\ e^{i\omega t} \quad \Im\ e^{i\omega t}] \times [\hat{x} \quad \hat{y}]^T, \qquad (2.9)$$

with the characterising constant T_2 describing the time where the signal strength has been reduced by a factor e^{-1}. This decay model is known as Free Induction Decay (FID) and assumes a perfectly homogeneous external magnetic field $B_0\hat{z}$.

The signal often decays faster than the FID-model predicts, which can be explained with the addition of extra dephasing sources in the shape of magnetic inhomogeneities, such as spatial variations in magnetic susceptibility, inhomogeneous field generated by the magnets, implants and other factors.

The combined effect from FID spin-spin interaction model and the additional dephasing from other sources is called T_2*-relaxation characterised by $1/T_2^* = 1/T_{2[\text{FID}]} + 1/T_{2[\text{other}]}$

The FID contributions are purely random events, but the fixed dephasing from other sources can be amended by exploiting the Spin-Echo (SE) effect. If reversibility of the fixed contributions is assumed, a phase-inversion at some time TE/2 will cause the dephasing caused by fixed sources cancel out and only the T_2-attenuated inverted signal remains at time TE/2+TE/2 = TE, known as the *echo time*.

2.5.1   Chemical shift

The chemical shift is the resonant frequency of a nucleon in a molecule related to the frequency of a nucleon in a reference molecule. The chemical shift artefact occurs when the local intramolecular environment such as lattice electron clouds partially screens the external field seen by the nuclei and perturbs the nuclear magnetodynamics, causing a shift in the Larmor frequency.

Factors impacting the measured shift include the local electron density and neighbour electronegativities. Different levels of screening from these effects create shifts in the Larmor frequency characteristic for the particular molecular structure. This artefact is exploited to obtain insight into the molecular composition of the sample. Some nuclei within a specific molecule can experience significantly different shifts, giving rise to multiple scattered peaks which all identify the same molecule.

The chemical shift δ is defined as $\delta = \frac{\nu_{\text{sample}} - \nu_{\text{ref}}}{\nu_{\text{ref}}}$, where ν_{sample} is the sample nucleon resonant frequency and ν_{ref} is the reference resonant frequency of the nucleon in the reference molecule. It is customary to state the chemical shift as parts per million (ppm) due to its low order of magnitude.

2.5.2   High resolution magic angle spinning MRS

HR-MAS MR is a type of spectroscopy that enables high resolution spectra to be be obtained with MRS of solid tissue(50). Normally, solid tissue MRS will produce spectra with quite broad peaks, caused by anisotropic interactions with a dependence on the orientation with respect to the external field. The effect is magnified by reduced mobility/motility of the cells compared to cells in liquids in that the ensemble average fails to cancel the effect simply by not being able to include a fully sampled distribution of all orientations. Thus, many of the interactions, in particular dipole-dipole interactions, are not properly averaged by internal motion, inducing angle dependent artefacts in the resulting spectra.

By tilting the sample to the magic angle and rotating about the new axis, the contributions from these interactions will be neglected, leading to narrowing of the peaks in the spectra and increased spectral resolution. The narrower the peaks, the easier to evaluate the spectrum and the quantitative analysis is significantly improved. An illustration of the principle is shown in fig. 2.7.
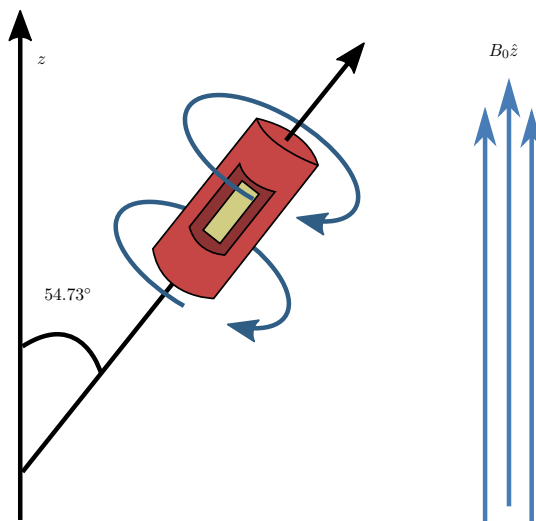
Figure 2.7: Illustration of HR-MAS MRS, where the sample is spun around an axis at an angle of $54.7°$ with respect to the magnetic field B_0.

2.5.3   Pulse sequences

There are several different sequences available for MR experiments, and the information one can obtain from each of them varies significantly, thus it is necessary to choose the sequence best suited for the characteristics of interest.

NOESY

1D and 2D Nuclear Overhauser Effect Spectroscopy (NOESY) is a homonuclear technique suitable for measuring cross-relaxation rates from ^{1}H in close proximity to other ^{1}H. In this method, the Nuclear Overhauser Effect (NOE) is used to measure correlations caused by transfer of spin polarisation by cross relaxation through intermolecular spin-lattice relaxation paths[51, 52] during mixing. NOESY is commonly used to study molecular structures.

The fundamental NOESY sequence is composed of three $90°$ pulses. The first pulse induces transversal magnetisation that evolves in a T_1 period. Further, another $90°$ pulse induces longitudinal magnetisation and in the following NOE mixing period, cross-relaxation occurs. Finally, a $90°$ pulse creates transverse magnetisation for detection. An example spectrum from a NOESY-experiment is show in fig. 2.8 A).

1D NOESY applies selective inversion or saturation to one peak and detects the NOE elsewhere. The sequence efficiently suppresses solvent signal, and McKay[53] provides a comprehensive review of 1D NOESY, discussing the importance and subtleties of the pulse sequence as well as outlining the benefits and drawbacks.

CPMG

Carr-Purcell-Meiboom-Gill (CPMG) is a pulse sequence that consists of successive $180°$ pulses following a $90°$ pulse at time intervals separated by 2τ. The sequence exploits the SE effect to cancel the dephasing effect from effects other than the stochastic FID. At intervals of period 2τ following the first inversion pulse, the individual phases refocus and generate a transient peak in the signal. The amplitude decay between successive peaks measures the T_2 rate. This allows for the inspection of T_2 relaxation times in the sample (T_2-filtering). In addition, transversal diffusion can be studied by varying the delay τ[54]. An example spectrum from a CPMG-experiment is show in fig. 2.8 B).
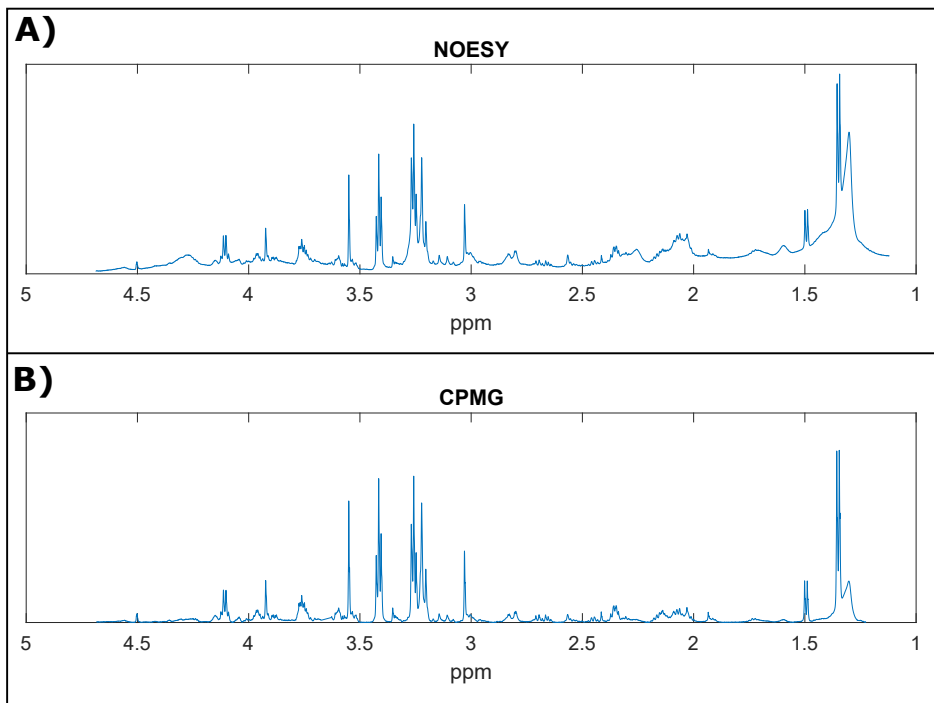
Figure 2.8: Example spectra from ^{1}H HR-MAS MRS acquisition using **A)** NOESY and **B)** CPMG pulse sequences.

JRES

J-resolved (JRES) is a hetero- and homonuclear experiment that separates the J-coupling from the chemical shift for multiplets by detecting the multiplet splitting(55). The experiment is able to detect and represent chemical shift and multiplicity in two dimensions, simplifying the analysis of complicated patterns by providing separation of multiplets in two axes.

The basic JRES sequence consists of a single $90°$ pulse to induce transversal magnetisation before the variable mixing time evolves the spins through chemical coupling and J-coupling. After half of the period, a $180°$ pulse is applied. This reverses the effect of the chemical shifts, but not the J-coupling at the end of mixing, at which the decay acquisition starts. (56) An example spectrum from a JRES-experiment is show in fig. 2.9. It has found applications in metabolomics(57).
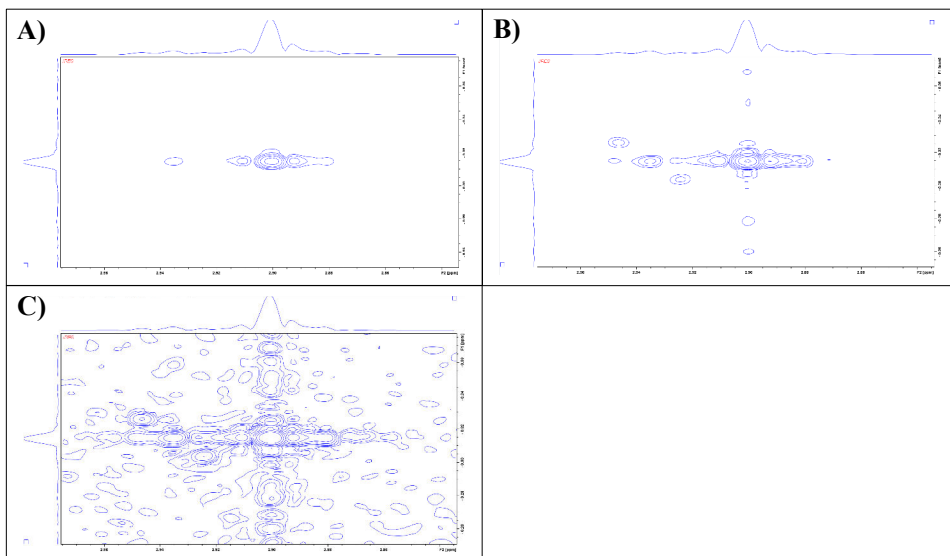
Figure 2.9: All three images (**A**)-**C**) are of the same 2D JRES spectrum, and illustrates how one can adjust the amount of information that is visible.

2.6   Spectral preprocessing methods

2.6.1   Asymmetric least squares baseline correction

Asymmetric Least Squares (ALS) uses a penalised weighted least squares approach to minimise systems of the form

$$\underset{x}{\mathrm{argmin}} \, ||\mathrm{diag}(\mathbf{w})(A\mathbf{x} - \mathbf{y})||^2 + \lambda^2||F\mathbf{x}||^2, \tag{2.10}$$

where A is the design matrix, λ is the penalty parameter, $\mathbf{w}$ is weights vector, $\mathbf{x}$ is the solution vector and $\mathbf{y}$ is the input vector. $|| \cdot ||$ denotes the Euclidean vector norm and $f(\mathbf{x}) = F\mathbf{x}$ is a linear function of the solution vector, indicating the cross-coupling between the solution components and giving rise to off-diagonal elements characteristic for the type of penalty imposed on the system.

This type of least squares formulation is readily solved by sparse software on modern computers in many applications.

Asymmetric weighting schemes for this method have been proposed in order to do baseline correction in spectrogram analysis. The idea is to use a switching weight

$$w_i = \begin{cases} 1 - p & x_i < y_i \\ p & y_i \leq x_i, \end{cases} \tag{2.11}$$

where p is the asymmetry parameter combined with a Whittaker smoother with second order differences penalisation(58). In this smoother, λ determines the smoothness of the solution vector. This establishes a smooth baseline solution that can be used to eliminate background noise in $\mathbf{y}$. Due to the solution dependence of the weighting factor, an iterative approach has to be employed. The feasibility and rapid convergence of this baseline correction method has been demonstrated by Eilers *et al.*(59) and we refer to Leslie R. Euceda *et al.*(60) for further discussion of its use in HR-MAS spectroscopy.

2.6.2   Probabilistic quotient normalisation

Probabilistic Quotient Normalisation (PQN), or median-fold change normalisation is a common method for normalising 1D Nuclear Magnetic Resonance (NMR) spectra(61).

A set of n perfectly phased, shimmed and baseline corrected(i.e., non-biased) 1D NMR spectra $\mathbf{x}$ can be expressed as

$$\mathbf{x} = \mathbf{ACS} + \mathbf{E}, \tag{2.12}$$

where $\mathbf{S}$ are the spectra as rows, $\mathbf{A} = \mathrm{diag}\{\alpha_1, \alpha_2, ..., \alpha_n\}$ is a diagonal matrix of dilution constants, $\mathbf{C}$ is the concentrations matrix and $\mathbf{E}$ is the noise matrix(62). The objective is to obtain $\mathbf{C}$ from $\mathbf{x}$, which requires an estimation of $\mathbf{A}^{-1}$,

$$\mathbf{C} = \mathbf{A}^{-1}(\mathbf{x} - \mathbf{E})\mathbf{S}^{-1}. \tag{2.13}$$

One common method uses the total spectral integrals to find the dilutions that normalise the concentrations(63). This method is hampered by spectra with an abundance of a certain compound. The large peaks caused by these compounds impacts the spectral integral, causing the computed concentrations from spectra with identical true concentrations outside the peak to appear variable. PQN circumvents this by computing the signal ratio for each shift to a reference spectrum and normalising each spectrum by the median ratio across all the shifts. This greatly neutralises the global dampening effect created by some overabundant compound in the sample and improves the concentration estimates.

2.6.3   Mean centred Pareto scaling

Prior to Multivariate Analysis (MVA), score transforms are often required. It is common to shift the data to zero mean or median and scale by some value related to the variance of the data.

Pareto scaling(64) is an autoscaling MVA pretreatment method which normalises the data through a z-scoring transformation by mean centring and scaling by the square root of the standard deviation,

$$\tilde{x}_{ik} = \frac{x_{ik} - \bar{x}_k}{\sqrt{s_k}},\tag{2.14}$$

where x_{ik} is the i-th sample of the k-th variable, $\bar{x}_k$ and s_k is the mean and standard deviation of variable k respectively and $\tilde{x}_{ik}$ score transformation. Many methods exist for scoring data in preparation of MVA; Pareto scaling retains data structure, reduces the relative importance of large features and is useful for enhancing small and medium variations in the data(65).

2.7   Principal component analysis

Pearson(66) was the first to describe PCA in 1901, and since then it has been further developed(67). It is an unsupervised MVA method for reducing the dimensionality of large data sets and enhancing data patterns using variance metrics of a set of multidimensional observations $\mathbf{x}^i$ collected as row vectors in a tall matrix X. The method projects the observations onto axes using a set of unit loading vectors $\mathbf{w}_k$ by the score transformation $t_k^i = \mathbf{w}_k \cdot \mathbf{x}^i$ in such a way that scores along axis k inherits maximum variance from X under the constraint that the axis is orthogonal to axes $1...k-1$. For axis k, the loading vector $\mathbf{w}_k$ can be computed as

$$\mathbf{w}_k = \underset{||\mathbf{w}||=1}{\operatorname{argmax}} \mathbf{w}^T \hat{X}^T \hat{X} \mathbf{w},\tag{2.15}$$

where $\hat{X} = X - \sum_{i=1}^{k-1} X \mathbf{w}_i \mathbf{w}_i^T$ is the data set with the preceding $k-1$ Principal Component (PC)s removed.

A scores plot is an image visualising two PCs of a data set to identify clusters that can be used as a basis for classification. Along with the scores plot it is useful to display a loadings plot to visually inspect which linear combinations produce the clusters.

3 | Methods

This chapter covers the experimental methods and data analysis protocols used working with this project. Fig. 3.1 outlines the steps that were performed.
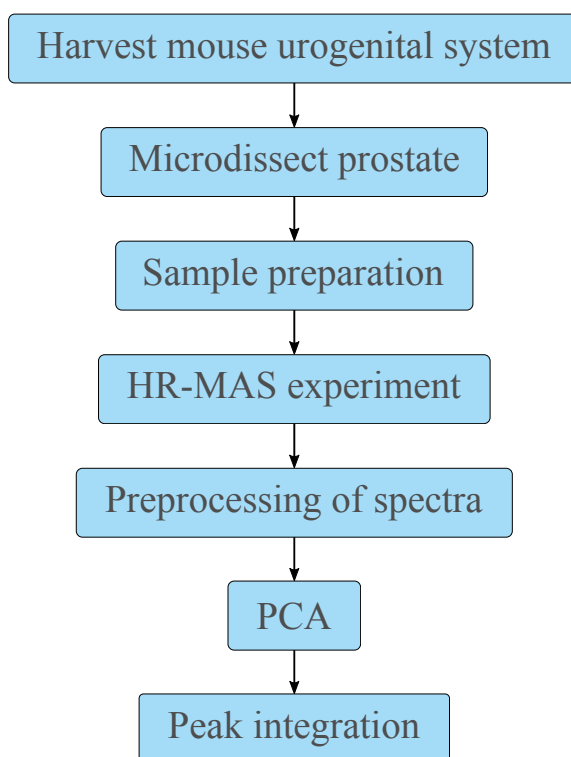
Figure 3.1: Outline of the experimental methods and data analysis that were part of this project.

3.1   Tissue samples

Tissue samples were obtained from both TRAMP and C57BL/6 (c57) mice. The background strain of the TRAMP model is c57, and one can therefore expect them to serve as a suitable healthy control. The mice were bred and housed at the Comparative Medicine Core facility, NTNU, St Olavs hospital, with unlimited access to standard rodent food (SDS RM1) and water. Both the TRAMP and the c57 mice are homozygote.

At the age of 32 ± 6 weeks (see table B.1 in the appendix for specifics) the mice were anaesthetised using isoflurane (Baxter, Norway) before they were euthanized by cervical dislocation. They were then dissected as shown in fig. 3.2 **A-B**, before the urogenital system was transferred into a dish (fig. 3.2 **C-D**), filled with phosphate buffered saline (10 Oxoid Phosphate Buffered Saline Tablets, Thermo Fischer Scientific Inc, USA dissolved in 1 l distilled water). The different lobes and any tumours were separated through microdissection[1]. All samples were snapfrozen in liquid nitrogen within 20 minutes, and stored in liquid nitrogen until they were prepared for HR-MAS MRS.
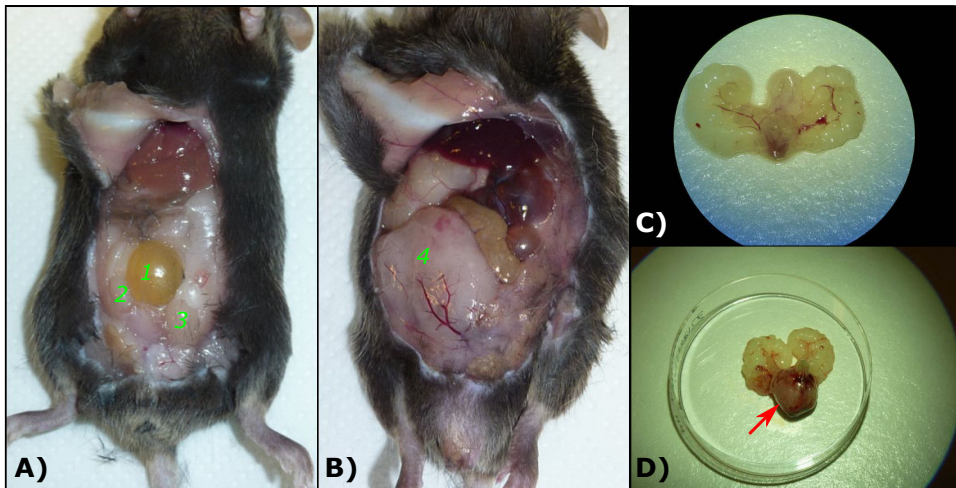
Figure 3.2: A) shows a c57 mouse where *1* indicates the bladder and *2+3* are the two testicles. The prostate is located behind these structures. **B)** is a TRAMP mouse with a large tumour marked as *4*, which covers the other anatomical structures that where visible in the healthy control. **C)** shows a normal looking urogenital system of a c57 mouse, while **D)** shows a urogenital system of a TRAMP mouse with a large tumour indicated by the red arrow. All photos: Deborah Katherine Hill.

---

[1]Performed by Dr. Deborah Katherine Hill

A two-tier grading system was used to classify samples from the TRAMP mice, where the two grades that were used were WD or PD. Since histopathology of the samples were not performed, this classification was based on how the prostate looked while dissecting, and not through histological images as is common. When visible tumours were present somewhere in the prostate, the samples were classified as PD. All other TRAMP mice were in this project classified as WD, as the ages at termination implies that cancer will have developed (100% of TRAMP mice develop cancer by 18 weeks of age(40)), though we might not always know in which parts of the prostate. A total of $n = 100$ samples from 27 mice were analysed, and how these were distributed between the different lobes and classifications is summarised in table 3.1. Histology will be performed on the HR-MAS samples, but it was not possible to complete this within the time constraint of this thesis.

Table 3.1: Overview of all the tissue samples from both the TRAMP and c57 mice. The samples from the TRAMP mice is divided into the two cancer classifications Poorly Differentiated (PD) and Well Differentiated (WD). Number of samples of LP = Lateral Prostate, AP = Anterior Prostate, DP = Dorsal Prostate and VP = Ventral Prostate is listed for both TRAMP and c57 mice. The tumour samples are from tumours in TRAMP mice that had grown to such an extent that it was difficult to with certainty determine where they arose, though the literature suggest that these PD tumours arise in the VP(43, 44).

	TRAMP			
	PD	WD	c57	*Sum*
LP	3	10	9	22
AP	1	10	9	20
DP	3	13	9	25
VP	3	11	10	24
Tumour	9	–	–	9
Sum	19	44	37	100

3.2 Sample preparation

A work station custom built for HR-MAS MRS sample preparation, shown in fig. 3.3, was used to prepare one sample at a time. The work station is made of polystyrene foam with a hole in the middle. Liquid nitrogen is poured into this hole to keep the sample frozen during sample preparation, preventing it from degrading. A metal plate is cooled down by soaking it in liquid nitrogen before it is placed directly on top of the hole, and a plexiglass plate is covering the rest of the work station to prevent the nitrogen from evaporating. A disposable weighing boat is then placed on top of the metal plate.
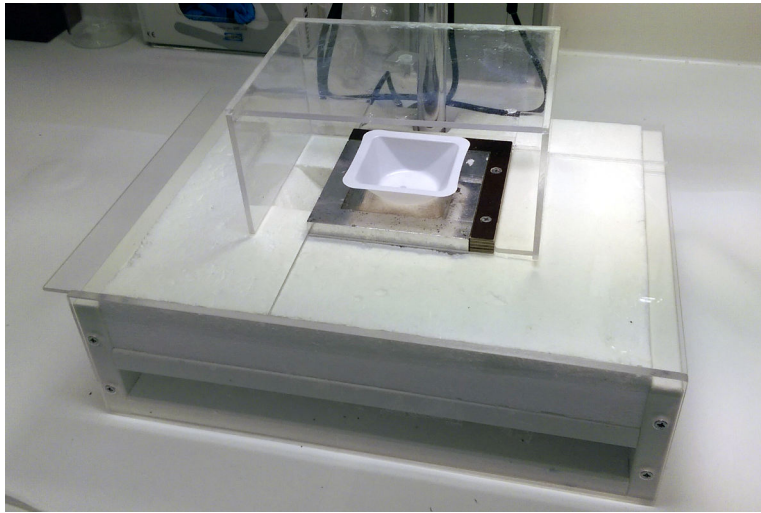
Figure 3.3: Workstation designed for HR-MAS MRS sample preparation. The polystyrene foam holds liquid nitrogen, and a cooled metal plate is placed on top. Plexiglass covering the rest of the work station prevents the nitrogen from evaporating. This ensures that degradation of the samples does not occur by keeping the sample frozen.

Into a disposable insert, $\sim 6\mu$l of a deuterium solution, consisting of deuterium oxide (D_2O 99.9%, CDN Isotopes, Quebec, Canada) mixed with sodium formate (HCOONa 99.998%, Sigma-Aldrich Chemie GmbH, Steinheim, Germany) to a concentration of 25mM HCOONa, were transferred. The samples were then cut to fit the inserts using a scalpel, as illustrated in fig. 3.4 **A)**. The weight of the samples were noted (mean weight were 9.1 ± 2.4 mg) in a lab sheet (fig. A.1 in appendix). The weights of both the samples and the added deuterium solution are listed in table B.1 in the appendix. The insert containing tissue and deuterium solution, as shown in fig. 3.4 **B)**, was sealed before it was transferred into a rotor (fig. 3.4 **C)**).
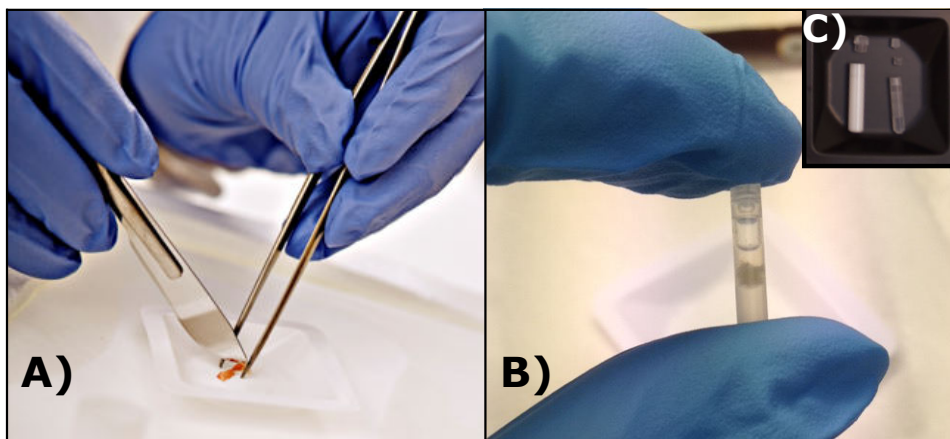
Figure 3.4: A) Picture of how the samples were cut to fit into the inserts. Photo: Geir Mogen/NTNU. **B)** An insert containing tissue sample and deuterium solution, ready to be put into a rotor. Photo: Silje Løveng **C)** A rotor (white) next to an empty insert. Photo: Tonje Haukaas.

3.3   HR MAS MRS experiments

A Bruker Avance DRX600 spectrometer (Bruker BioSpin GmbH, Germany) equipped with a ^{1}H/^{1}13C MAS probe was used for the ^{1}H HR-MAS MRS experiments. The rotors were transferred by a Sample PRO (Bruker BioSpin GmbH, Germany) into the magnet where they were spun at 5 kHz and kept at 5°C.

Tuning and matching were performed for each sample to ensure a sharp and centred wobble signal. The magnet was locked to the signal from the D_2O solution surrounding the tissue in order to prevent drift in in the spectra.

Shimming was performed by adjusting the current through the shim coils until the shape and width of the formate peak was satisfactory. Average shim was 1.13 ± 0.48 Hz.

$P1$ (the 90° pulse) was determined by estimating a value for $4 \cdot P1$, which equals a 360° pulse. Changing this value until the signal was ~ 0 gave the $P1$. $O1$ was also adjusted for each sample to achieve good suppression of the water signal. This was done by trial and error until the water signal was sufficiently weak. Both $P1$ and $O1$ are listed for all samples in table B.1 in the appendices.

NOESY (noesygppr1d, Bruker Biospin, GmbH, Germany), CPMG (cpmgpr1d, Bruker Biospin, GmbH, Germany) and JRES (jresgpprqf, Bruker Biospin, GmbH, Germany) spectra were acquired for all samples, with parameters specified in table

3.2 and the pulse sequence diagrams in fig. 3.5 **A)-C)**, which were obtained from the built in PulseProg feature in TopSpin 3.1 (Bruker BioSpin, GmbH, Germany). The average time spent inside the magnet was 100 ± 27 min.

Table 3.2: Overview of HR-MAS MRS acquisition parameters (D = relaxation delay, AQ = acquisition time, NS = number of scans and SW = spectral width) for all three pulse sequences. JRES parameters are presented as F2/F1, with F2 being the horizontal axis and F1 the vertical axis in the JRES spectra.

Pulse sequence	D (s)	AQ (s)	NS	SW (ppm)
NOESY	4.00	2.74	128	-10 to 20
CPMG	4.00	3.07	256	-5 to 15
JRES	2.00	0.41/0.26	1	-3.5 to 13/-0.25 to -0.38

Figure 3.5: Pulse sequence diagrams with time intervals and FIDs indicated. **A)** The NOESY experiment. **B)** The CPMG experiment. **C)** The JRES experiment.

3.4 Preprocessing of data

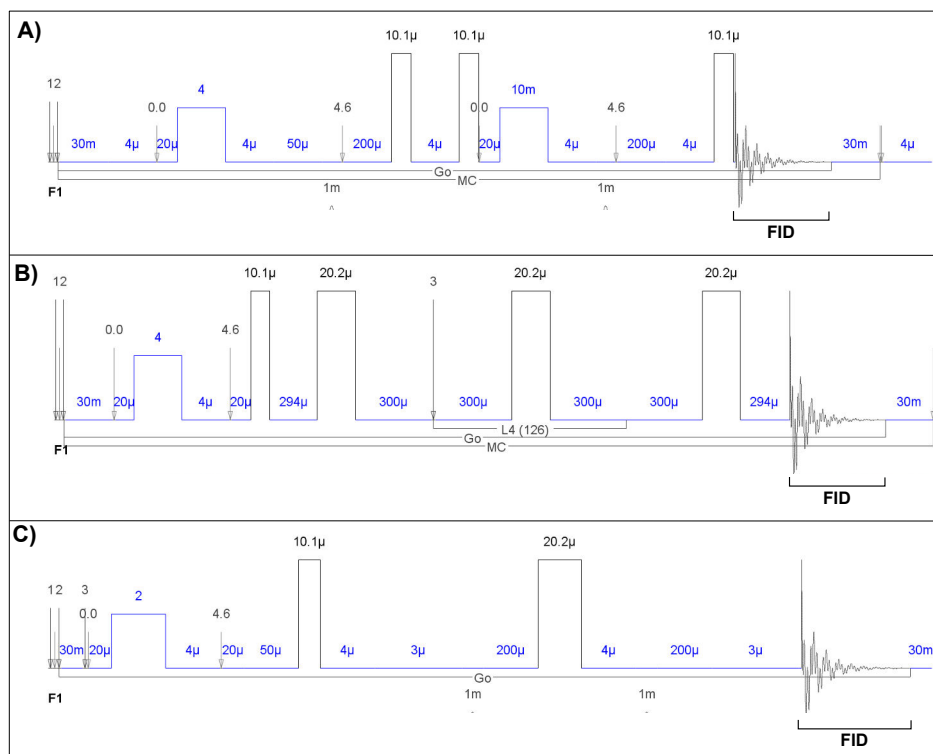Preprocessing needs to be performed in order to reduce the effects that any instrumental or experimental artefacts will introduce. In TopSpin 3.1 (Bruker BioSpin, GmbH, Germany) automatic phase correction was applied on all spectra. MATLAB R2016a (The MathWorks, Inc., USA) was used for the rest of the preprocessing.

For this project the CPMG spectra were chosen, as this will reduce the effect of larger molecules such as lipids with its T_2 filtering, enabling easier detection of smaller molecules.

First step in the preprocessing was shifting the spectra with respect to the creatine peak to achieve better alignment. The spectra were then cut to a suitable Region of Interest (ROI) where the metabolites one wanted to study would be located. Based on similar experiments previously performed(36)(68), the ROI was set to $1.2 - 4.7$ ppm.

The creatine and glycine peaks were used as reference when creating the ppm scale, which was done by assigning these two peaks to the ppm values 3.03 and 3.55, respectively.

Baseline correction was done in two steps. First, the lowest point in all the spectra was set to zero, and then ALS correction was performed on all spectra. The smoothing parameter γ was set to 10^{-7}, and the asymmetry parameter p was set to 10^{-5}.

Ethanol was detected as a contaminant in some spectra. One of the peaks from ethanol were cut of when the ROI was chosen, and the second peak at $\sim 3.63 - 3.67$ ppm was removed by eliminating the data at this interval.

To improve the peak alignment, *i*coshift(69) was applied for the data of c57 samples. When *i*coshift was tested with the data set for all $n = 100$ samples, the algorithm introduced glaring artefacts such as evident misalignment due to large variations within the dataset. Within the c57 samples there were less variations, and the application of *i*coshift gave improved alignment of the metabolite peaks. In the analysis of the data, peak alignment was therefore not used when studying all $n = 100$ samples at once, but for analysis investigating only the c57 samples, the *i*coshifted c57 data set was used.

Identification of the metabolites within the spectra was mostly done based on existing literature from similar experiments(36)(68) and on information from the Human Metabolome Database(70), but Chenomx Profiler (Chenomx, Inc,. Edmonton, Canada) was also used.

Built-in functions of the PLS Toolbox (Eigenvector Research, Inc., Washington, USA) for MATLAB were used to perform the normalisation and scaling. PQN was chosen as this has been proven to be a robust method for metabonomics studies(61). Pareto scaling was then applied, as this scaling method will affect dominating metabolites more than the ones that are less abundant(71). This will prevent these dominating metabolites to be the only ones showing in the results of the PCA, as the variations in the less abundant metabolites will be accentuated. Despite this accentuating, one does not risk to amplify any noise in the spectra with pareto scaling(64), and the shape of the data will be close to the original one(71). The data was also mean-centered to reduce the multicolinearity and get a better fit of the model(72).

3.5 Spectral analysis

3.5.1 Principal component analysis

The PLS Toolbox was used for the PCA. Analysis was performed on the complete data set with all $n = 100$ samples, and for c57 and TRAMP mice separately. Built-in cross-validations in the PLS toolbox were found to be a good choice, and contiguous blocks with number of splits $s = 5$ were therefore used.

Scores plots for all $n = 100$ samples combined were made both with labels of classification (c57, WD, PD) and of lobes, as well as both of these labels combined. Scores plots for c57 were labelled with lobes, and for TRAMP the labels were the lobes and tumour.

3.5.2 Quantification - Peak integration

Relative concentrations of metabolites that were prominent in the PCA were found through peak integration, which was performed in MATLAB. For the metabolites that show up as more than one peak in the spectra, the mean of the integration across the different peaks was used. Even though lactate have two peaks within the ppm range that was chosen as the ROI for this project, only the peak at ~ 4.1 ppm was included, as the other peak at ~ 1.35 ppm was overlapping with lipids.

3.6 Histology

Histology images of the different lobes of both healthy and diseased mouse prostate were obtained from previously Haemotoxylin Eosin Saffron (HES) stained tissue

sections(43)[2], as histology of the actual tissue samples used in this thesis was not performed at the time of writing. This was done in order to look for differences in the luminal spaces of diseased prostate, as are found in healthy mouse prostate(14). Any variations in citrate concentrations of different lobes may be explained by such differences, as this is where citrate is accumulated(73).

For minimum 48 hours, the Genitourinary (GU) tract had been fixed in 10% formalin before it was embedded in paraffin. Tissue sections were then cut to a thickness of 4μm. Using an automatic slide-stainer (Sakura Tissue-Tek Prisma, the Netherlands), the tissue sections were then stained with hematoxylin (ChemiTeknik, Norway), erythrosin (Sigma-Aldrich, Norway) and saffron (ChemiTeknik, Norway).

An Olympus BX41 microscope (Olympus Optical Co. (Europa), GMBH, Hamburg, Germany) with 10x magnification was used for the acquisition of the images. Images were acquired of all four lobes from both a c57 mouse (31.3 weeks at termination), from a TRAMP mouse with WD PCa (31.6 weeks at termination), and from a PD tumour of a TRAMP mouse (13.7 weeks at termination, tumour in VP).

---

[2]Performed by Dr. Deborah Katherine Hill.

4 | Results

In this section the results will be presented, first with example spectra from different samples, and then with figures showing the outcome of the PCA and the peak integration.

4.1 Spectral data

The spectra with highest correlation within the classes PD, WD and c57 are presented in fig. 4.1. The PD spectrum is of a tumour centre, the WD is from an AP and the c57 is a DP. Differences in the metabolite peaks are evident. In fig. 4.2 **A)-C)** the spectra with the highest correlation within the DP and VP samples of the PD, WD and c57 are plotted, and this figure too is included to show differences in the spectra. Fig. 4.3 shows a representative spectrum where metabolites have been assigned to the corresponding peaks, with the metabolites listed in table 4.1. The spectrum is obtained from a VP in a c57 mouse.
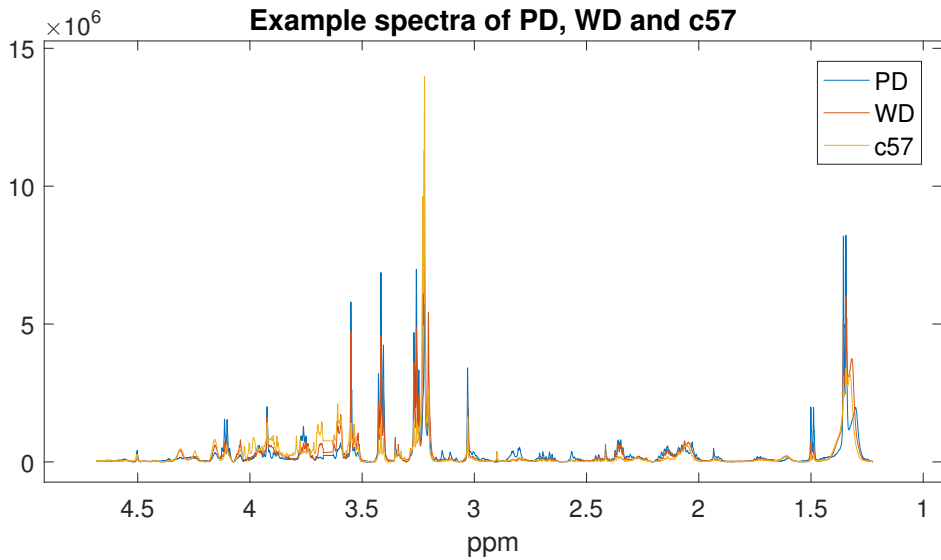
Figure 4.1: The best corresponding spectra from each of the three classes PD, WD and c57 plotted together. The PD spectrum is of a tumour centre, the WD is from an AP and the c57 is a DP. Baseline correction, shifting of spectra with respect to creatine peak and removal of ethanol $(3.63 - 3.67$ ppm) have been performed on all the spectra.
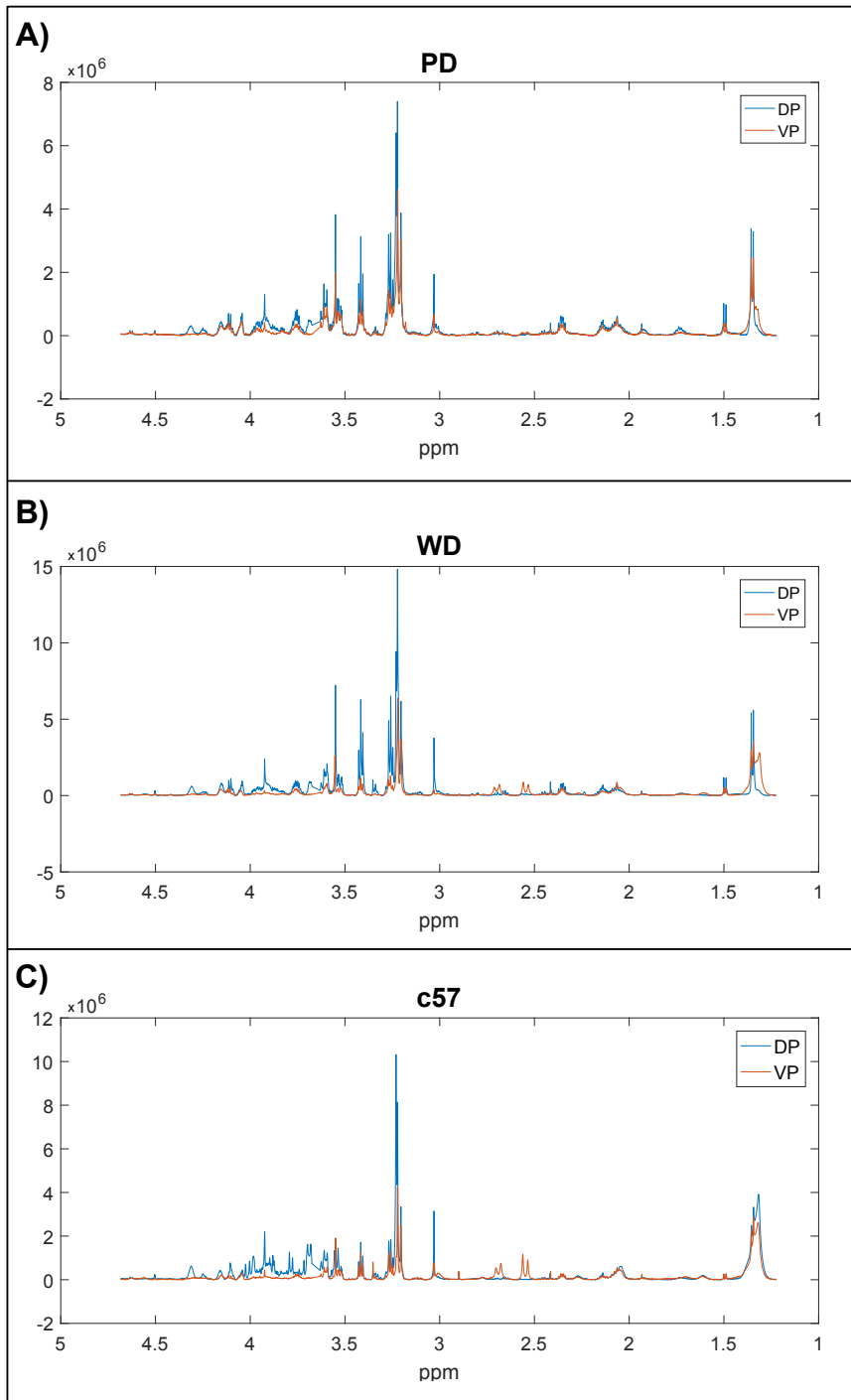
Figure 4.2: The best corresponding spectra of DP and VP samples from each of the three classes **A**) PD, **B**) WD and **C**) c57. Baseline correction, shifting of spectra with respect to creatine peak and removal of ethanol ($3.63 - 3.67$ ppm) have been performed on all the spectra.

Spectra with metabolites
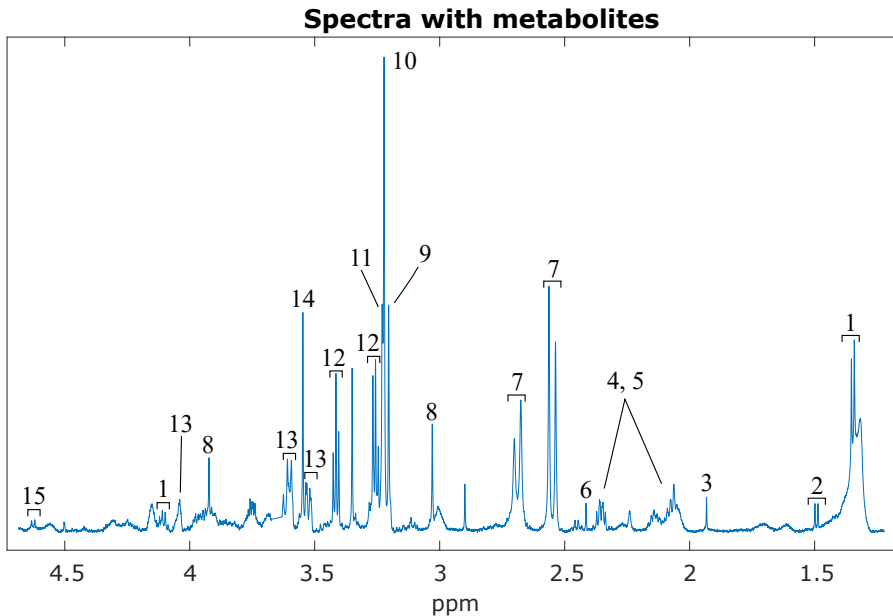
Figure 4.3: A representative spectrum with the main metabolites assigned, with the assigned metabolites listed in table 4.1. The spectrum is obtained from a VP sample of a c57 mouse. Baseline correction, shifting of spectra with respect to creatine peak and removal of ethanol $(3.63 - 3.67$ ppm$)$ have been performed on all the spectra.

Table 4.1: List of the metabolites that are assigned in the spectrum in fig. 4.3.

Peak	Metabolite	Peak	Metabolite
1	Lactate	9	Choline
2	Alanine	10	Phosphocholine
3	Acetate	11	GPC
4	Glutamate	12	Taurine
5	Glutamine	13	Myo-inositol
6	Succinate	14	Glycine
7	Citrate	15	β-glucose
8	Creatine		

4.2 Principal Component Analysis

This section will present the results of the PCA of the whole dataset and of TRAMP and c57 separated. Both scores plot and loadings plot will be shown for all relevant PCs. In PC5 and higher the variance within the data sets were too small to tell if

the variations were random, and no clear grouping could be seen. These PCs were therefore not included in in this exploratory project.

All samples combined

Scores plots and loadings plots for the PCA that included all $n = 100$ samples are shown in subsection 4.2.1. The samples were first labelled by cancer classification (PD, WD and c57). Fig. 4.4 **A)** shows the scores plot for the first and second PCs, while the corresponding loadings plots are shown in **B)-C)**, respectively. In the loadings plots, the horizontal axis is the same ppm scale as the original data sets had. The peaks that are at positive PC values in the loadings plots represent the metabolites that are high in the samples located at positive values for the same PC in the scores plot. In fig. 4.5 **A)** results of the third and fourth PCs are plotted, with the loadings plots for PC3 and PC4 in fig. 4.5 **B)-C)**. Scores plot for PC2 and PC3 combined are given in fig. 4.6 **A)**, while the combination of PC2 and PC4 can be seen in fig. 4.6 **B)**. The same results were also labelled after which prostate lobe the samples were from, and fig. 4.7 **A)-B)** and 4.8 **A)-B)** shows these scores plots. A third way of labelling the samples are shown in fig. 4.9, where the samples were labelled both with prostate lobe as well as if its TRAMP or c57. The loadings plots accompanying all these scores plots are the same as for the other scores plots (fig. 4.4 **B)-C)** and 4.5 **B)-C)** where all $n = 100$ samples are included. Fig. 4.10 shows an example of another type of loadings plot, in which the loadings of two PCs are combined, that were used as a complement to the previously mentioned type of loadings plot. In this figure it is the PC2 and PC4 that are plotted. The most prominent metabolites are assigned directly in the figure. These loadings plots were used to identify the metabolites that caused the largest variations, and they make it easier to identify which samples that correlates with these metabolites. In these loadings plots, the metabolites at a certain location in the loadings plot are high in samples that are located in the corresponding area in the scores plot.

Lobes in c57

The results of the PCA that was performed on only c57 samples to investigate differences between the different prostate lobes are given in subsection 4.2.2. The scores plot for the two first PCs along with their loadings plots are shown in fig. 4.11 **A)-C)**. The scores plot for the third and fourth PCs are given in fig. 4.12 **A)**, with the loadings plots of the two PCs in fig. 4.12 **B)-C)**. Fig. 4.13 **A)** and **B)** shows the scores plots for PC2 combined with PC3 and PC2 combined with PC4, respectively. The loadings plots shown for the other scores plots of c57 samples also corresponds to these last two scores plots.

Lobes/tumour in TRAMP

In subsection 4.2.3 the results of the PCA of the TRAMP samples are presented. Scores plot for PC1 and PC2 with corresponding loadings plots are shown in fig. 4.14 **A)-C)**, and scores plot for PC3 and PC4 are shown in fig. 4.15 **A)** with their loadings plots in **B)-C)**. Finally, fig. 4.16 gives the scores plot for **A)** PC2 combined with PC3 and **B)** PC2 combined with PC4. The loadings plots in the two previous figures for the TRAMP samples applies for these two last scores plots as well.

4.2.1   Figures from the PCA of all samples
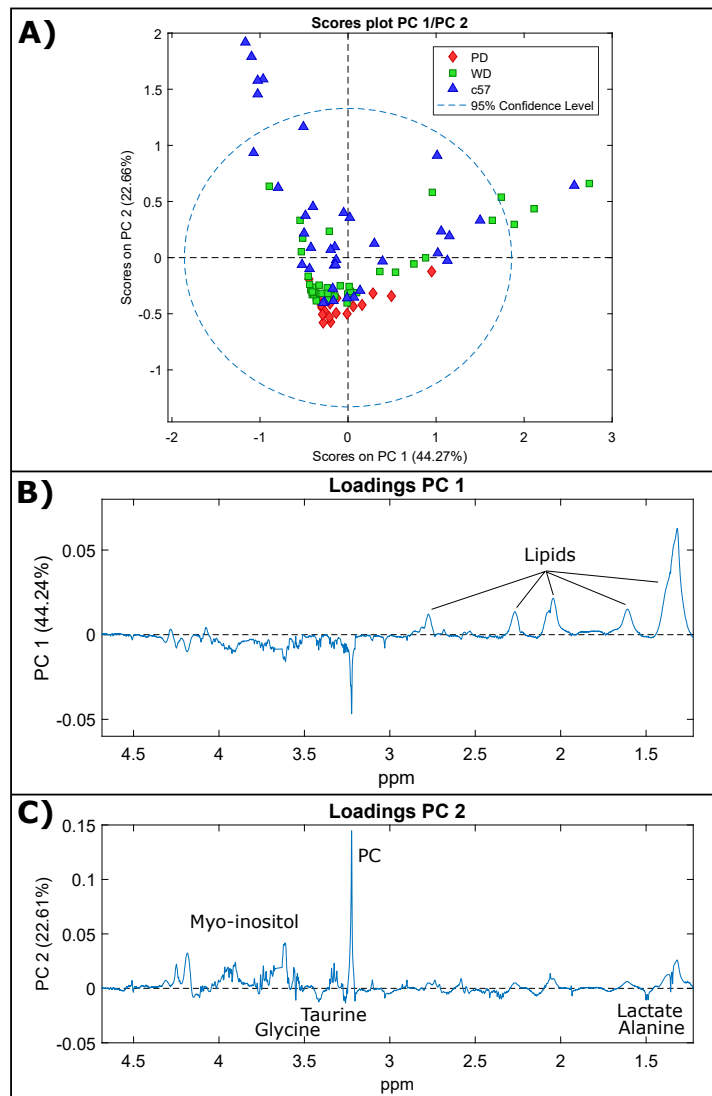
Figure 4.4: A) The scores plot for all $n = 100$ samples plotted with their scores on PC1 along the horizontal axis and PC2 on the vertical axis. The samples are labelled as c57 and the two classes of TRAMP, where the PD samples are shown as red diamonds, WD samples are the green squares and the blue pyramids are the c57 samples. The dotted circle shows the 95% confidence level, which indicates the 2 standard deviations limit in the inherited variance. **B)** shows the loadings plot for PC3 and **C)** shows the loadings plot for PC4. The metabolite peaks pointing in the direction of positive PC x are high in the samples that are located at positive PC x in the scores plot, and the peaks at negative PC x are high in samples at negative PC x in the scores plot.

Figure 4.5: A) The scores plot for all $n = 100$ samples plotted with their scores on PC3 along the horizontal axis and PC4 on the vertical axis. The samples are labelled as c57 and the two classes of TRAMP, where the PD samples are shown as red diamonds, WD samples are the green squares and the blue pyramids are the c57 samples. The dotted circle shows the 95% confidence level, which indicates the 2 standard deviations limit in the inherited variance. **B)** shows the loadings plot for PC1 and **C)** shows the loadings plot for PC2. The metabolites pointing in the direction of positive PC x are high in the samples that are located at positive PC x in the scores plot, and the peaks at negative PC x are high in samples at negative PC x in the scores plot.
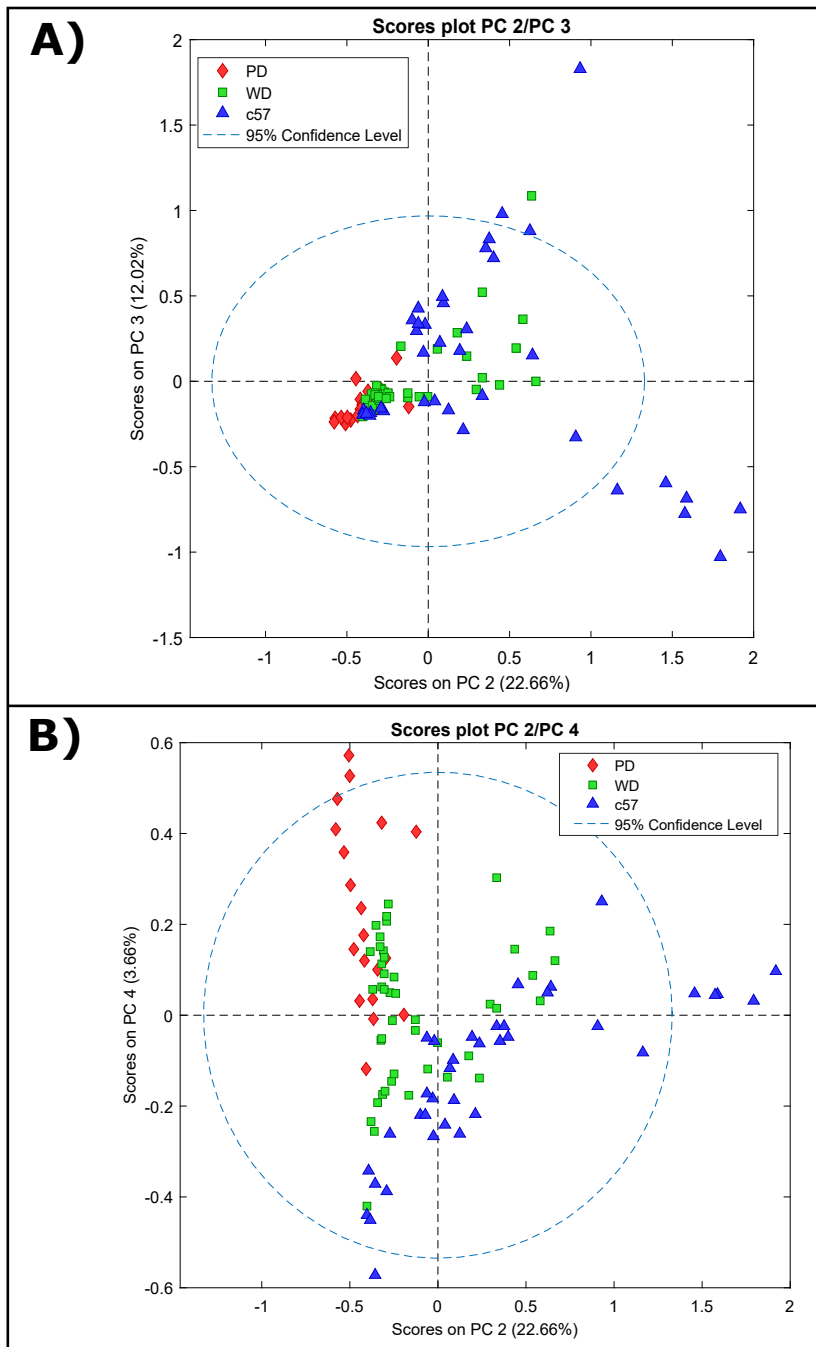
Figure 4.6: The figure shows two different scores plot with all $n = 100$ samples, labelled by classification. **A)** shows the PC2 along with PC3, while **B)** is the scores plot for PC2 and PC4. The PD samples are shown as red diamonds, WD samples are the green squares and the blue pyramids are the c57 samples. The dotted circle shows the 95% confidence level, which indicates the 2 standard deviations limit in the inherited variance.
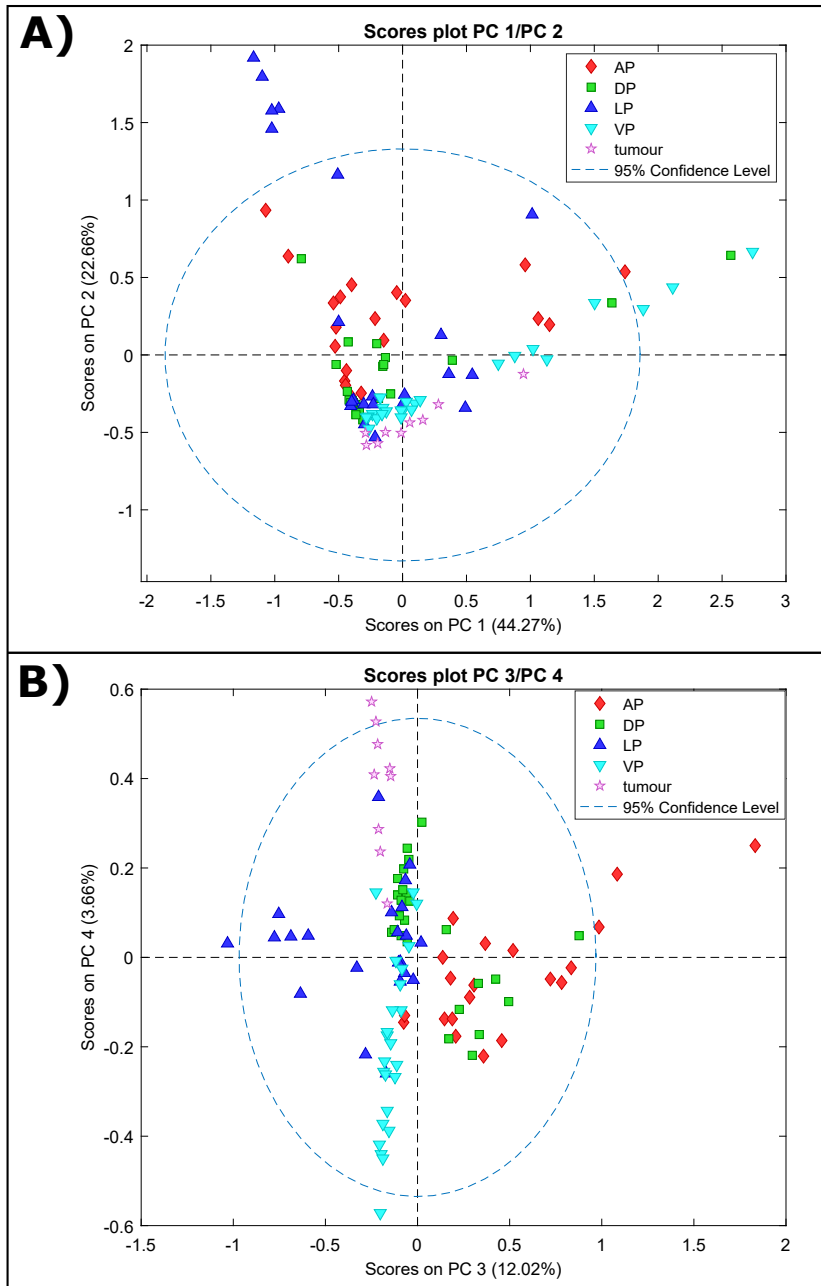
Figure 4.7: The figure shows two different scores plot with all $n = 100$ samples, labelled by prostate lobe. **A)** shows the PC1 along with PC2, while **B)** shows PC3 and PC4. The AP samples are plotted as red diamonds, the DP samples are the green squares, LP samples are the blue pyramids, VP samples are the turquoise nablas while the pink stars are the tumour samples. The dotted circle shows the 95% confidence level, which indicates the 2 standard deviations limit in the inherited variance.
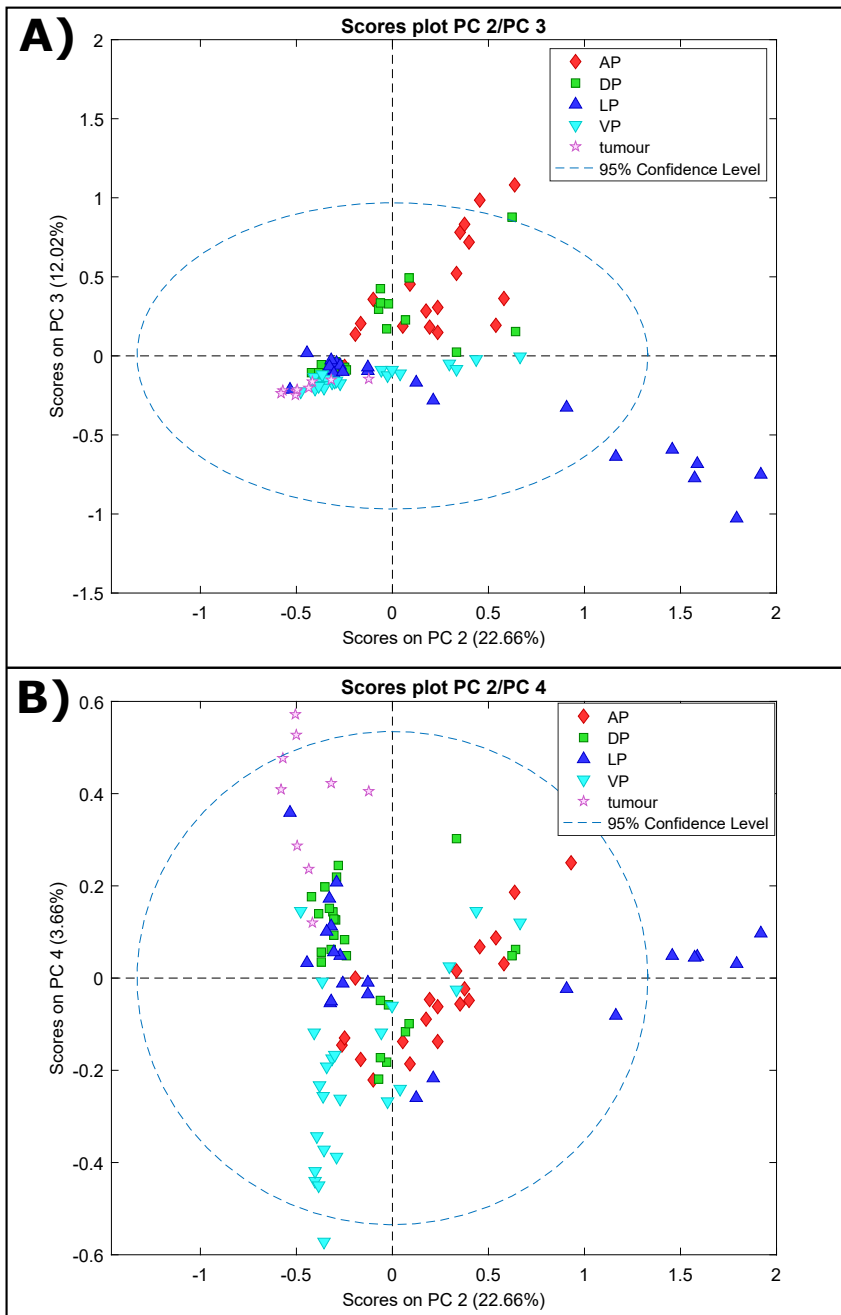
Figure 4.8: The figure shows two different scores plot with all $n = 100$ samples, labelled by prostate lobe. **A)** shows the PC2 along with PC3, while **B)** shows PC2 and PC4. The AP samples are plotted as red diamonds, the DP samples are the green squares, LP samples are the blue pyramids, VP samples are the turquoise nablas while the pink stars are the tumour samples. The dotted circle shows the 95% confidence level, which indicates the 2 standard deviations limit in the inherited variance.
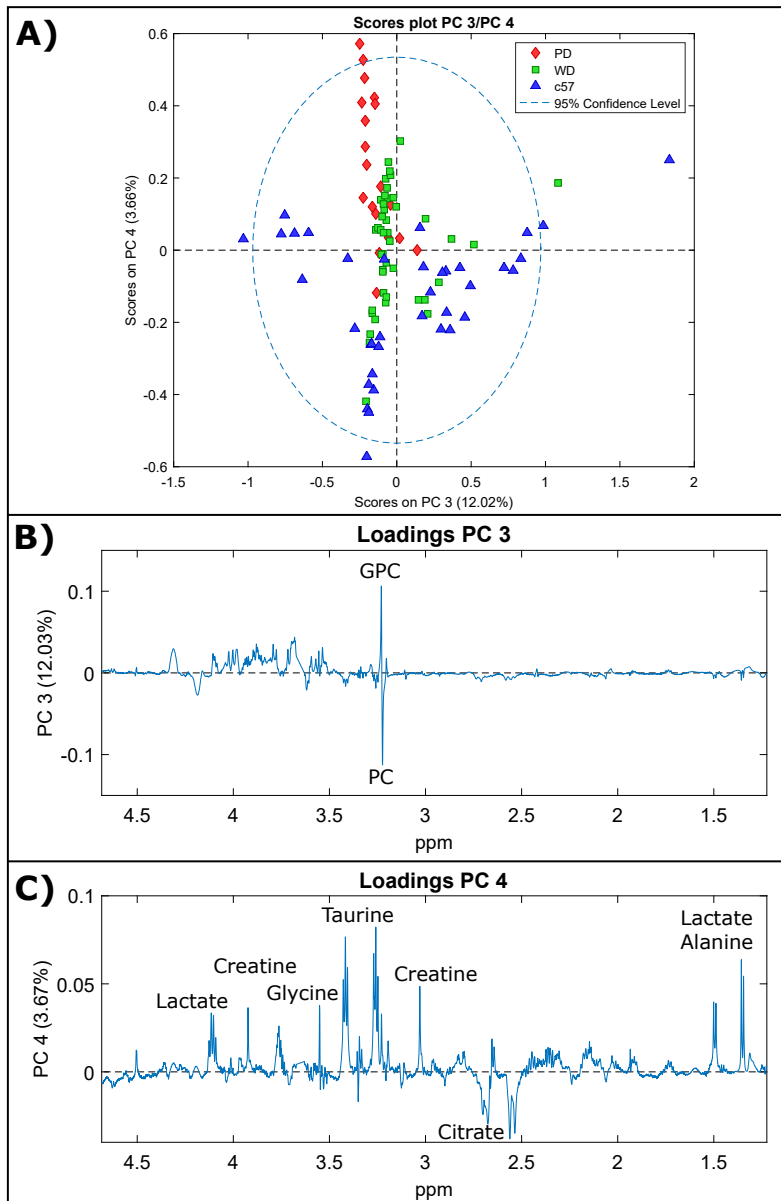
Figure 4.9: The scores plot for all $n = 100$ samples plotted with their scores on PC2 along the horizontal axis and PC4 on the vertical axis. The samples are labelled by prostate lobe, where the TRAMP samples are separated from the c57 samples by being plotted as only the contours of the markers, while the c57 samples are coloured in. The AP samples are plotted as red diamonds, the DP samples are the green squares, LP samples are the blue pyramids, VP samples are the turquoise nablas while the pink stars are the tumour samples. The dotted circle shows the 95% confidence level, which indicates the 2 standard deviations limit in the inherited variance.
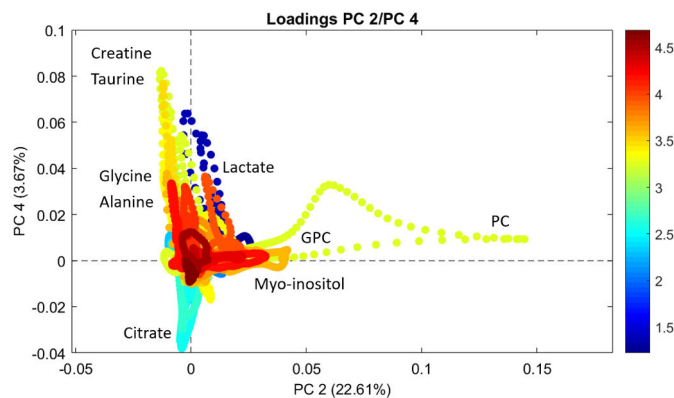
Figure 4.10: Loadings plot of PC2/PC4 for the PCA performed on all $n = 100$ samples. The colouring represent ppm, and the metabolites at a certain location in the loadings plot are high in the samples that are located at the corresponding area in the scores plots with PC2 and PC4 (fig. 4.6 **B)**, 4.8 **B)**, 4.9). The most prominent metabolites in the plot are labelled directly in the figure.

4.2.2 Figures from the PCA of c57 samples

Figure 4.11: A) The scores plot for the PCA of only the c57 samples plotted with their scores on PC1 along the horizontal axis and PC2 on the vertical axis. The samples are labelled by prostate lobe, where the AP samples are plotted as red diamonds, the DP samples are the green squares, LP samples are the blue pyramids and the VP samples are the turquoise nablas. The dotted circle shows the 95% confidence level, which indicates the 2 standard deviations limit in the inherited variance. **B)** shows the loadings plot for PC1 and **C)** shows the loadings plot for PC2. The metabolite peaks pointing in the direction of positive PC x are high in the samples that are located at positive PC x in the scores plot, and the peaks at negative PC x are high in samples at negative PC x in the scores plot.

Figure 4.12: A) The scores plot for the PCA of only the c57 samples plotted with their scores on PC3 along the horizontal axis and PC4 on the vertical axis. The samples are labelled by prostate lobe, where the AP samples are plotted as red diamonds, the DP samples are the green squares, LP samples are the blue pyramids and the VP samples are the turquoise nablas. The dotted circle shows the 95% confidence level, which indicates the 2 standard deviations limit in the inherited variance. **B)** shows the loadings plot for PC3 and **C)** shows the loadings plot for PC4. The metabolite peaks pointing in the direction of positive PC x are high in the samples that are located at positive PC x in the scores plot, and the peaks at negative PC x are high in samples at negative PC x in the scores plot.

Figure 4.13: Two different scores plot for the PCA of only the c57 samples, labelled by prostate lobe. **A)** shows the PC2 along with PC3, while **B)** shows PC2 and PC4. The AP samples are plotted as red diamonds, the DP samples are the green squares, LP samples are the blue pyramids and the VP samples are the turquoise nablas. The dotted circle shows the 95% confidence level, which indicates the 2 standard deviations limit in the inherited variance.
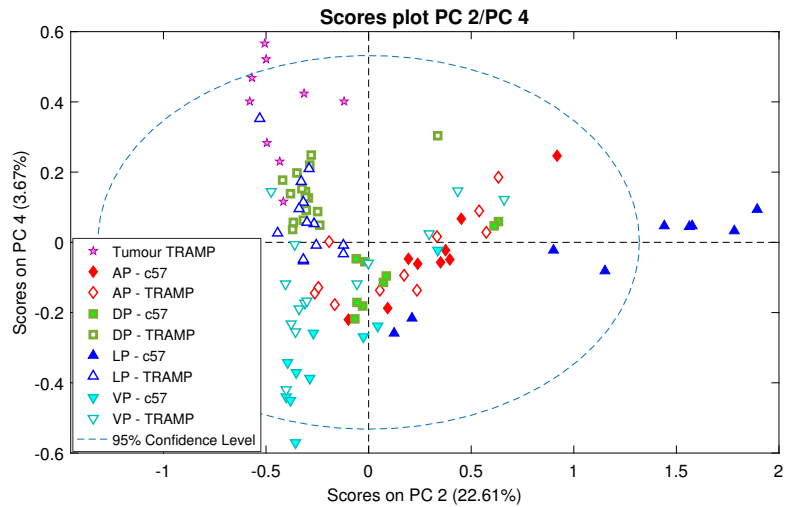
4.2.3   Figures from the PCA of TRAMP samples
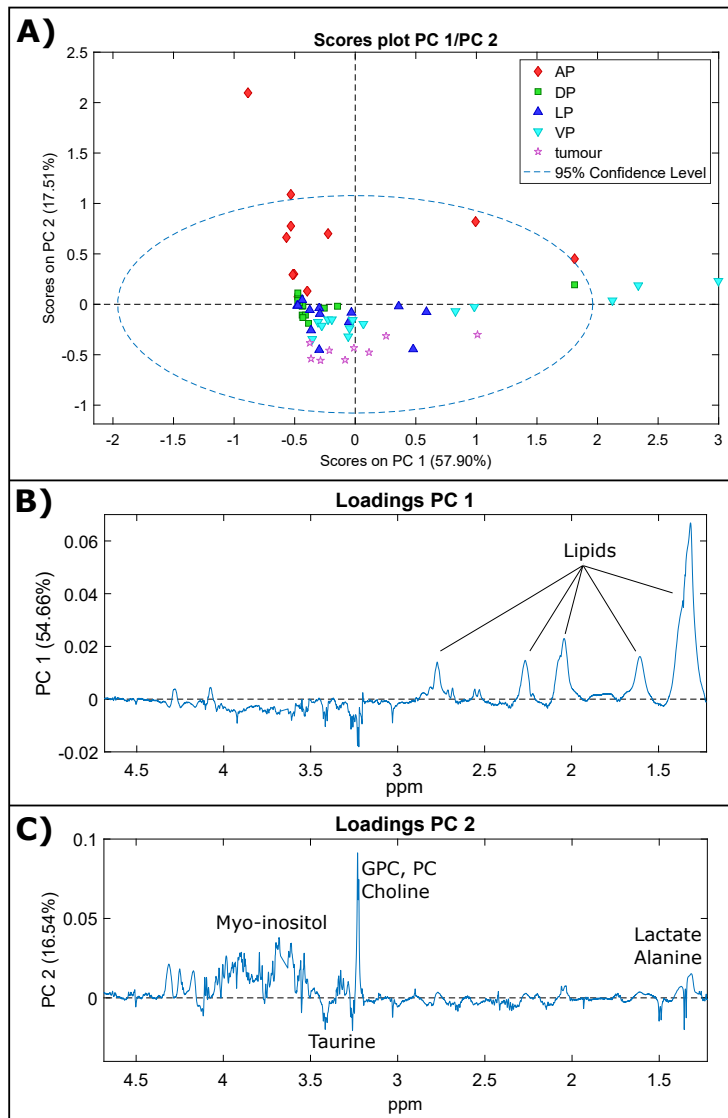
Figure 4.14: A) The scores plot for the PCA of only the TRAMP samples plotted with their scores on PC1 along the horizontal axis and PC2 on the vertical axis. The samples are labelled by prostate lobe, where the AP samples are plotted as red diamonds, the DP samples are the green squares, LP samples are the blue pyramids, the VP samples are the turquoise nablas and the pink stars are the tumour samples. The dotted circle shows the 95% confidence level, which indicates the 2 standard deviations limit in the inherited variance. **B)** shows the loadings plot for PC1 and **C)** shows the loadings plot for PC2. The metabolite peaks pointing in the direction of positive PC x are high in the samples that are located at positive PC x in the scores plot, and the peaks at negative PC x are high in samples at negative PC x in the scores plot.
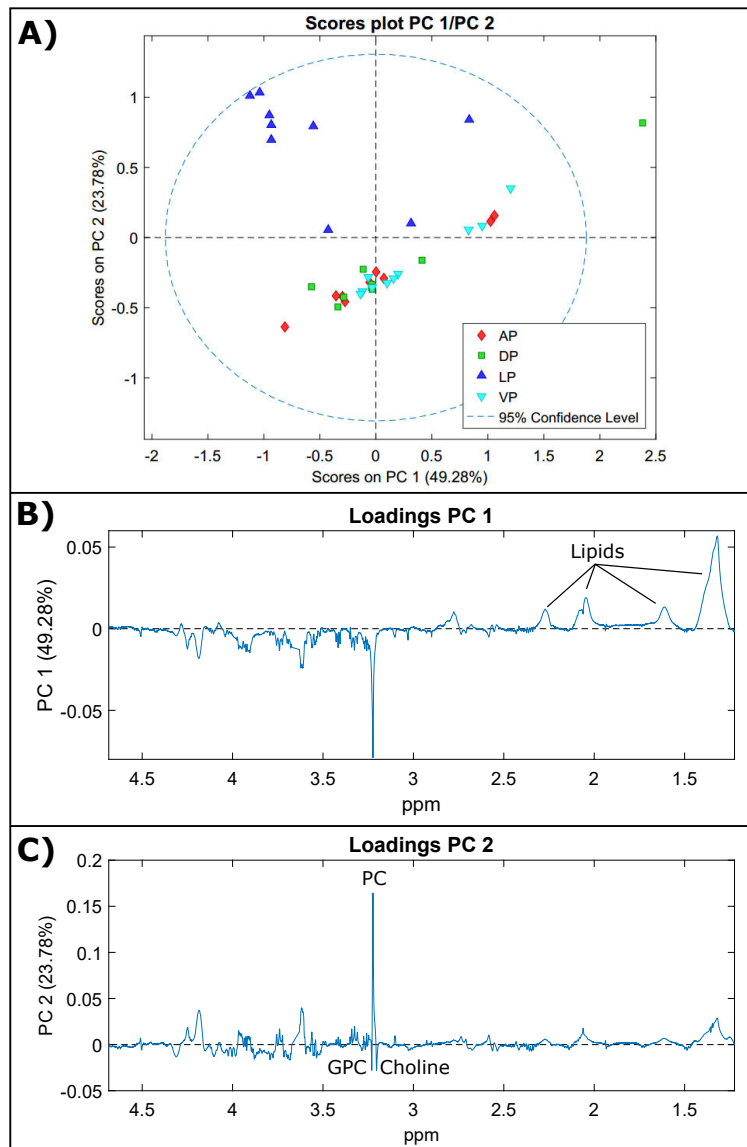
Figure 4.15: A) The scores plot for the PCA of only the TRAMP samples plotted with their scores on PC3 along the horizontal axis and PC4 on the vertical axis. The samples are labelled by prostate lobe, where the AP samples are plotted as red diamonds, the DP samples are the green squares, LP samples are the blue pyramids, the VP samples are the turquoise nablas and the pink stars are the tumour samples. The dotted circle shows the 95% confidence level, which indicates the 2 standard deviations limit in the inherited variance. **B)** shows the loadings plot for PC3 and **C)** shows the loadings plot for PC4. The metabolite peaks pointing in the direction of positive PC x are high in the samples that are located at positive PC x in the scores plot, and the peaks at negative PC x are high in samples at negative PC x in the scores plot.
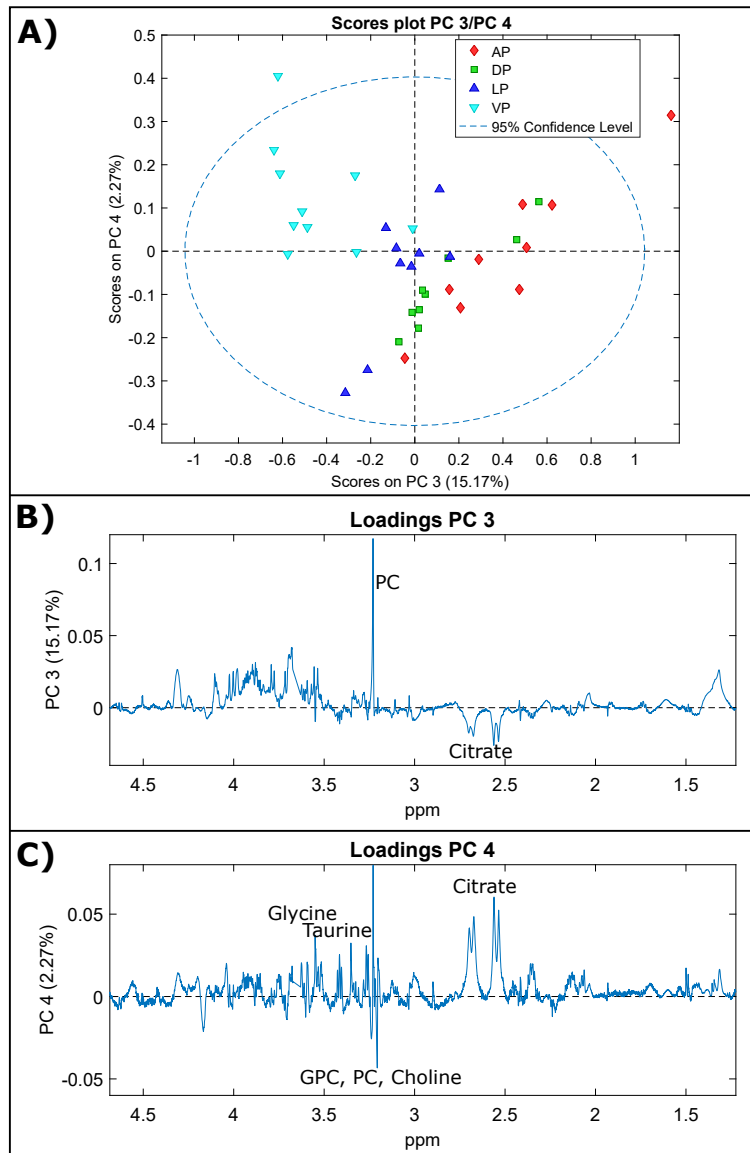
Figure 4.16: Two different scores plot for the PCA of only the TRAMP samples, labelled by prostate lobe. **A)** shows the PC2 along with PC3, while **B)** shows PC2 and PC4. The AP samples are plotted as red diamonds, the DP samples are the green squares, LP samples are the blue pyramids and the VP samples are the turquoise nablas. The dotted circle shows the 95% confidence level, which indicates the 2 standard deviations limit in the inherited variance.

4.3   Peak Integration

The relative concentrations of metabolites that were found through integration across chosen peaks of the spectra are presented as bar plots in this section. Each bar represents the mean concentration within the given classes and lobes, with

empirical standard deviation indicated with error bars.

Relative concentrations of chosen metabolites (lactate, glycine, alanine, taurine, GPC, phosphocholine and citrate), based on the most prominent metabolites in the PCA, are shown in fig. 4.17 **A)** for all c57, PD and WD samples. The metabolites with the lowest concentrations in this figure are plotted together in 4.17 **B)** to better visualise the differences between the bars.

In fig. 4.18 **A)** the relative concentrations of the same metabolites as previously listed are shown for each lobe of only the c57 samples, and in **B)** the ones with lowest concentrations are plotted again to better see the variances in bar height.

The five metabolites that showed the most variations in concentrations between different lobes in fig. 4.18 are plotted again in fig. 4.19 **A)-E)**, this time for both c57, WD and PD and for all four lobes. The PD tumour samples are excluded. A reminder of the mouse prostate anatomy can be seen in fig. 4.19 **F)**. Fig. 4.20 shows the relative concentrations of these five metabolites for PD tumour samples, with c57 VP samples for comparison as it is suggested that this is where the PD tumours originate(43)(74)(44).
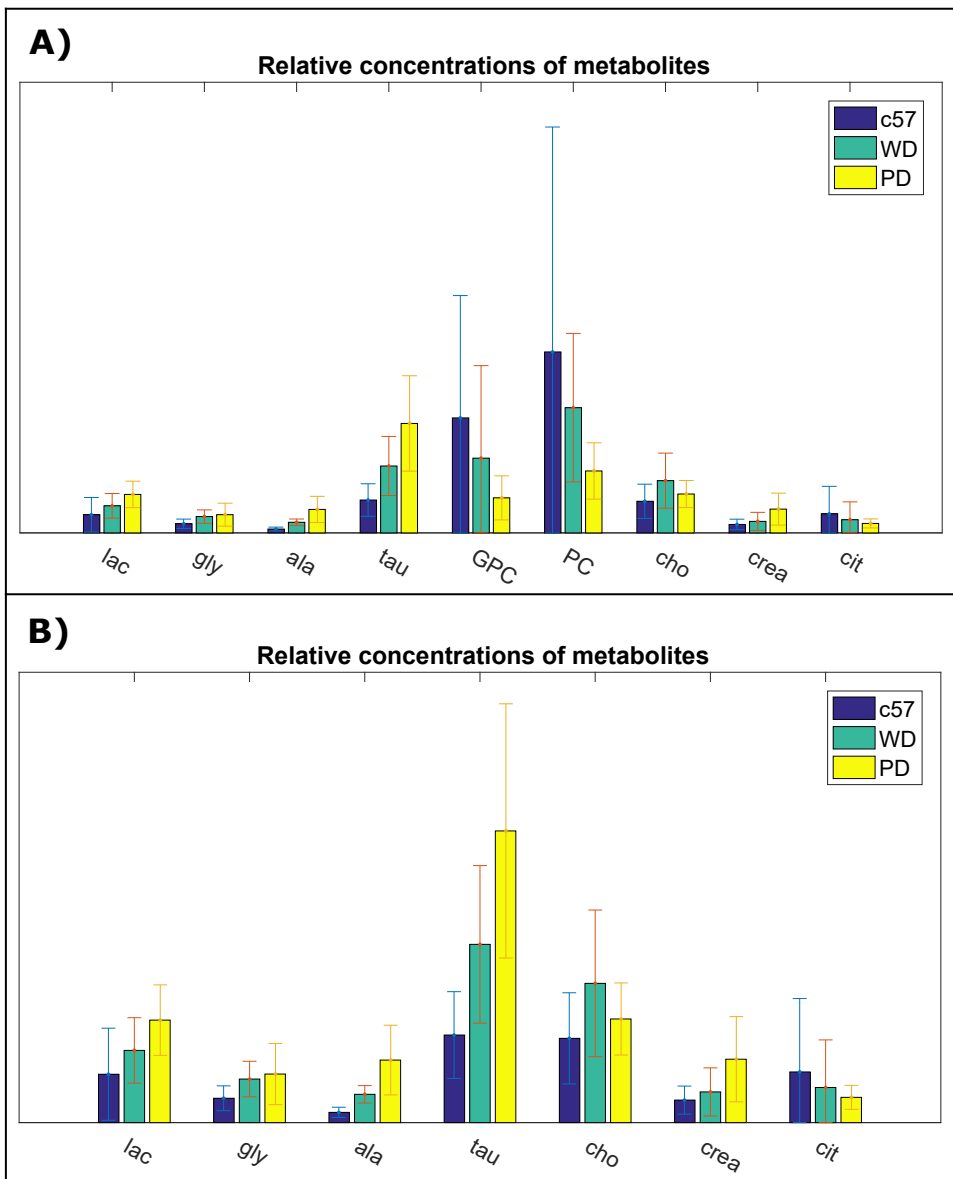
Figure 4.17: A) Relative concentrations of metabolites within PD, WD and c57 samples, found through integration across the spectra, of important metabolites in different classes of samples. Blue bars represent the data for c57, green bars are the WD samples, and yellow are PD samples. Corresponding standard deviation is plotted along with all bars. The metabolites that are plotted are lactate (lac), glycine (gly), alanine (ala), taurine (tau), glycerophosphocholine (GPC), phosphocholine (PC), choline (cho), creatine (crea) and citrate (cit). **B)** The metabolites with lower concentrations in the top spectra plotted to better see the variations between the different lobes.
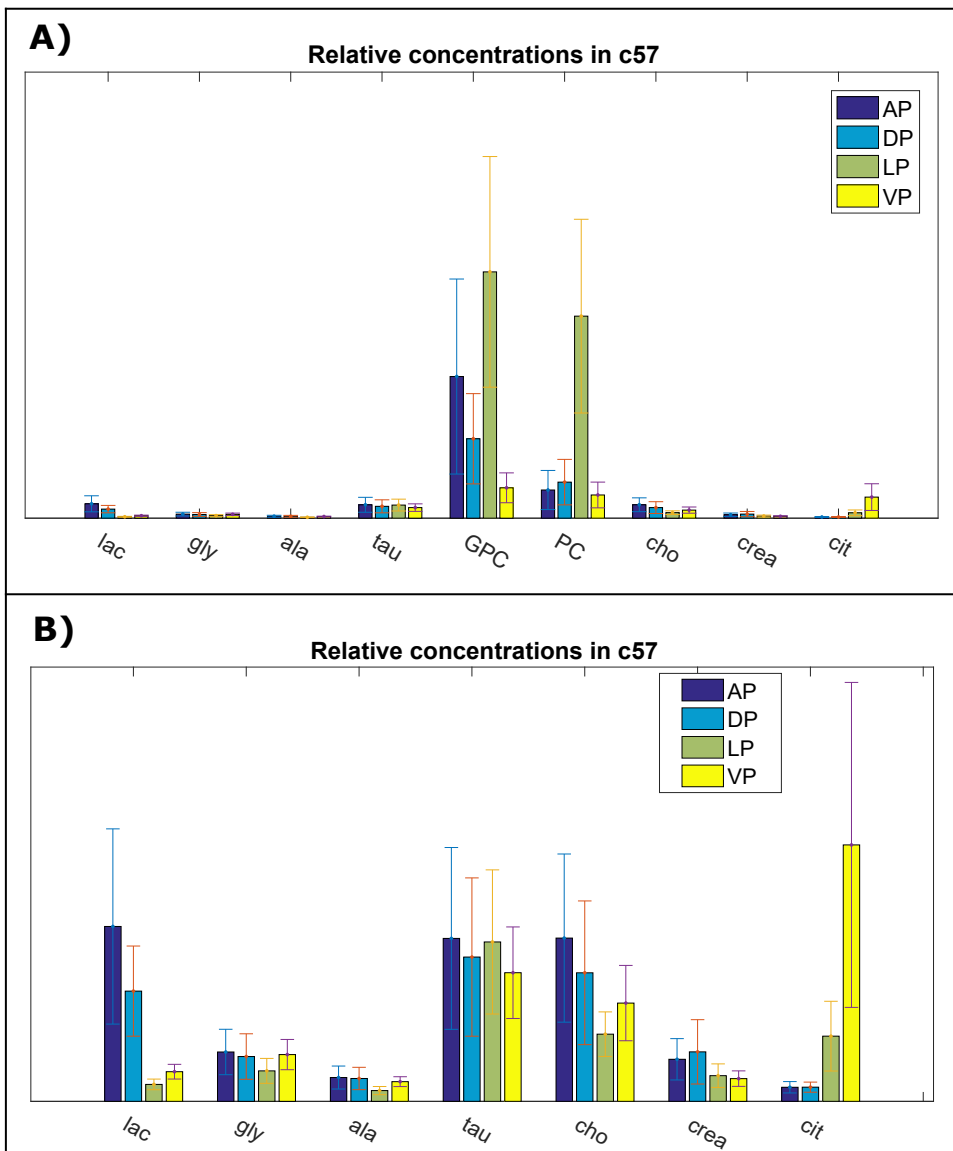
Figure 4.18: A) Relative concentrations of important metabolites in the prostate lobes of c57 mice, found through integration across the spectra. The mean value for AP samples are shown in dark blue, DP samples are lighter blue, LP samples are green and yellow bars are the VP samples. Corresponding standard deviation is plotted along with all bars. The metabolites that are plotted are lactate (lac), glycine (gly), alanine (ala), taurine (tau), glycerophosphocholine (GPC), phosphocholine (PC), choline (cho), creatine (crea) and citrate (cit). **B)** The metabolites with lower concentrations in the top spectra plotted to better see the variations between the different lobes.
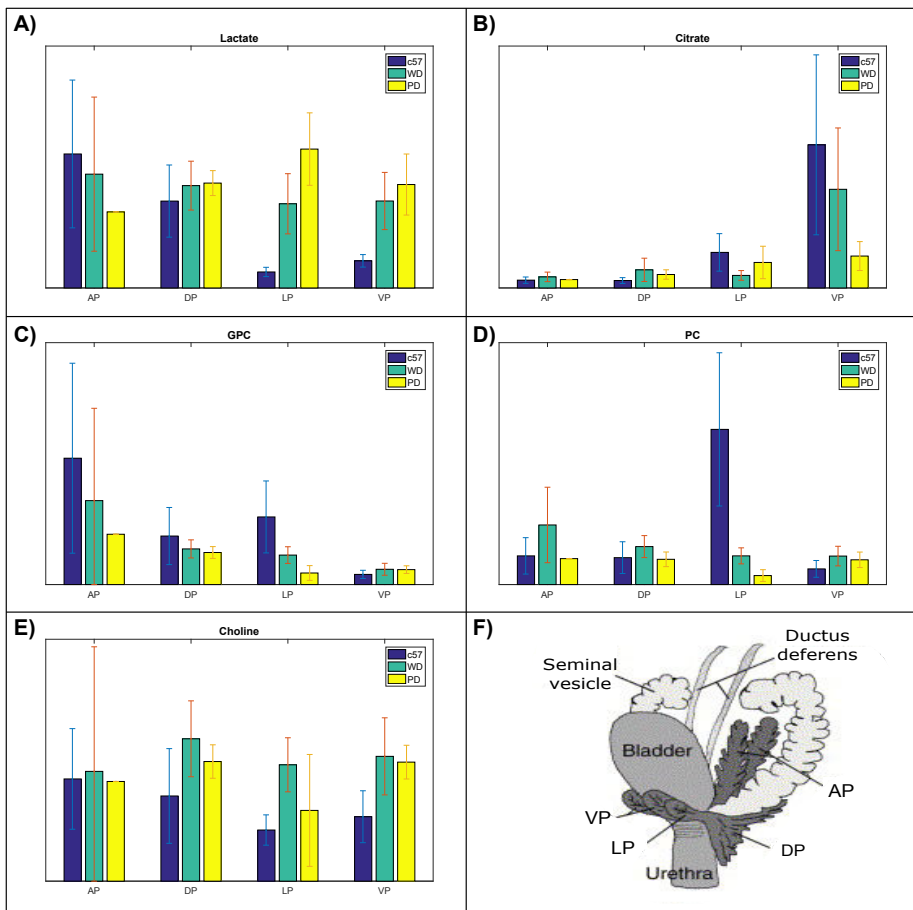
Figure 4.19: Relative concentrations of metabolites within the different prostate lobes of PD, WD and c57 mice, found through integration across the spectra, of important metabolites in different lobes of all three classes. PD tumour samples are excluded. Blue bars represent the mean concentration for c57, green bars are the WD samples, and yellow are PD samples. Corresponding standard deviation is plotted along with all bars. The metabolites that are plotted are **A)** lactate (lac), **B)** citrate, **C)** glycerophosphocholine (GPC), **D)** phosphocholine (PC) and **E)** choline. In **F)** an illustration of the mouse prostate anatomy is shown.
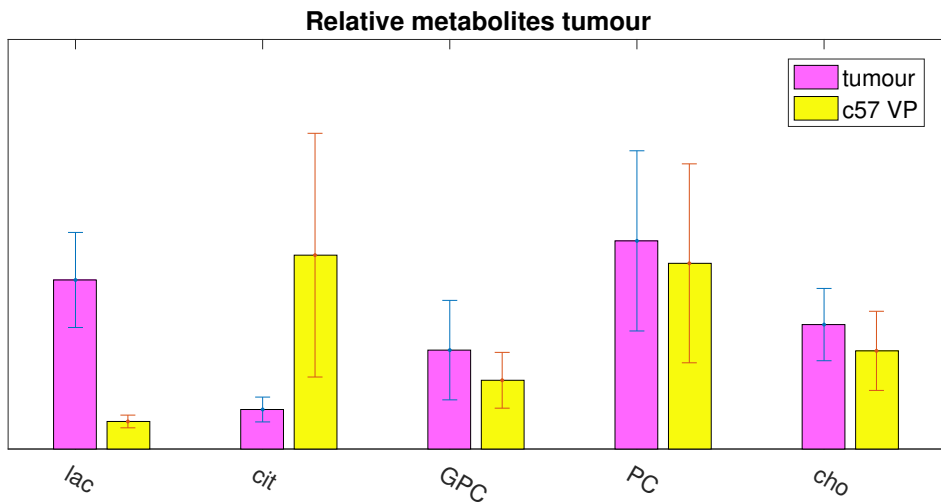
Figure 4.20: Relative concentrations of metabolites in PD tumour (pink) compared to c57 VP (yellow), found through integration across the spectra. Corresponding standard deviation is plotted along with all bars. The metabolites that are plotted are lactate (lac), citrate (cit), glycerophosphocholine (GPC), phosphocholine (PC) and choline (cho).

4.4   Histology

Histology images that were obtained from a previous study on TRAMP and c57 mice are presented in this section. Representative images of the four lobes of the prostate in a TRAMP mouse are shown in 4.21 **A)-D)**, and an image of a PD tumour can be seen in 4.21 **E)**. Images of the four different lobes from a c57 mouse are shown in fig. 4.22 **A)-D)**.
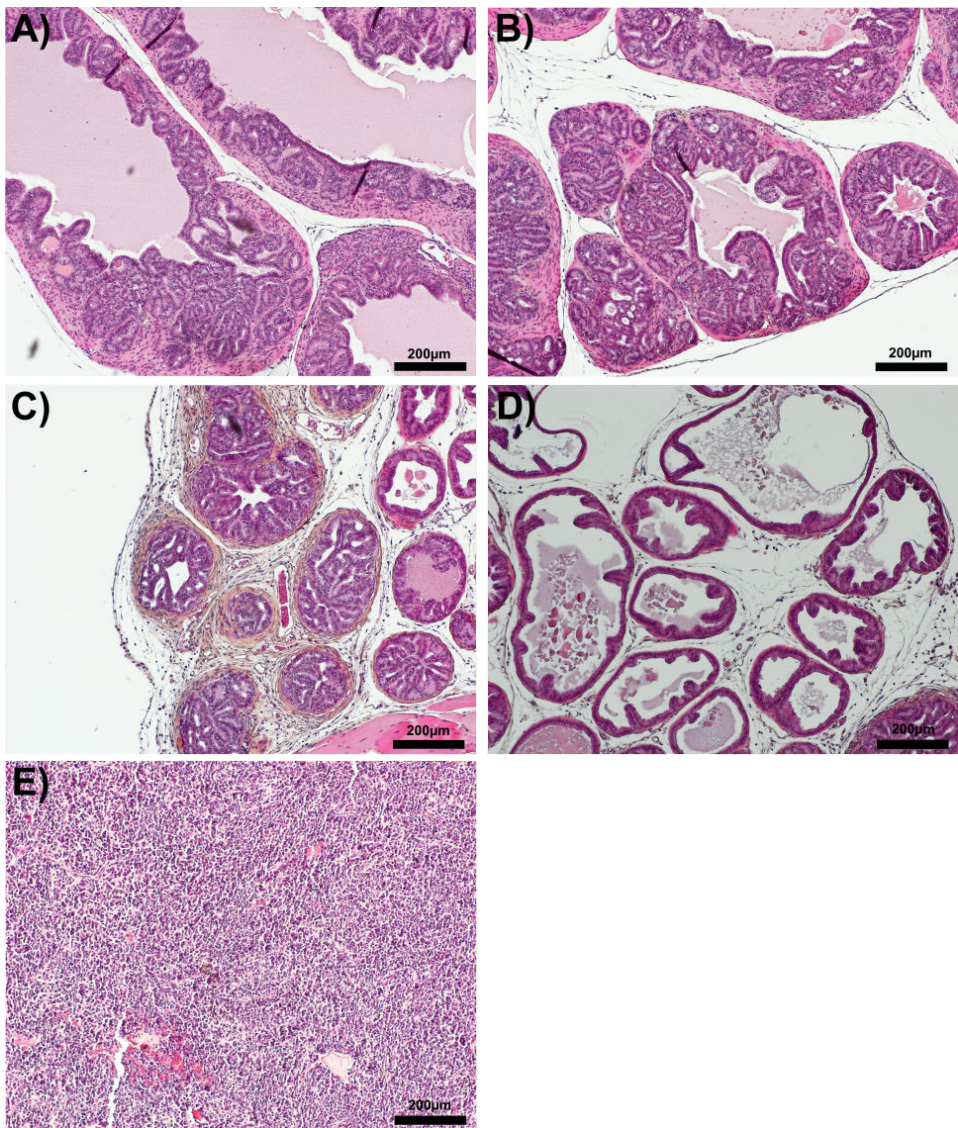
Figure 4.21: Histology images of HES stained tissue sections from TRAMP mice. **A)** is the AP, **B)** is the DP, **C)** is the LP and **D)** is the VP. All four slices are from the same mouse with PCa classified as WD. **E)** shows an image of a PD tumour from a different mouse.
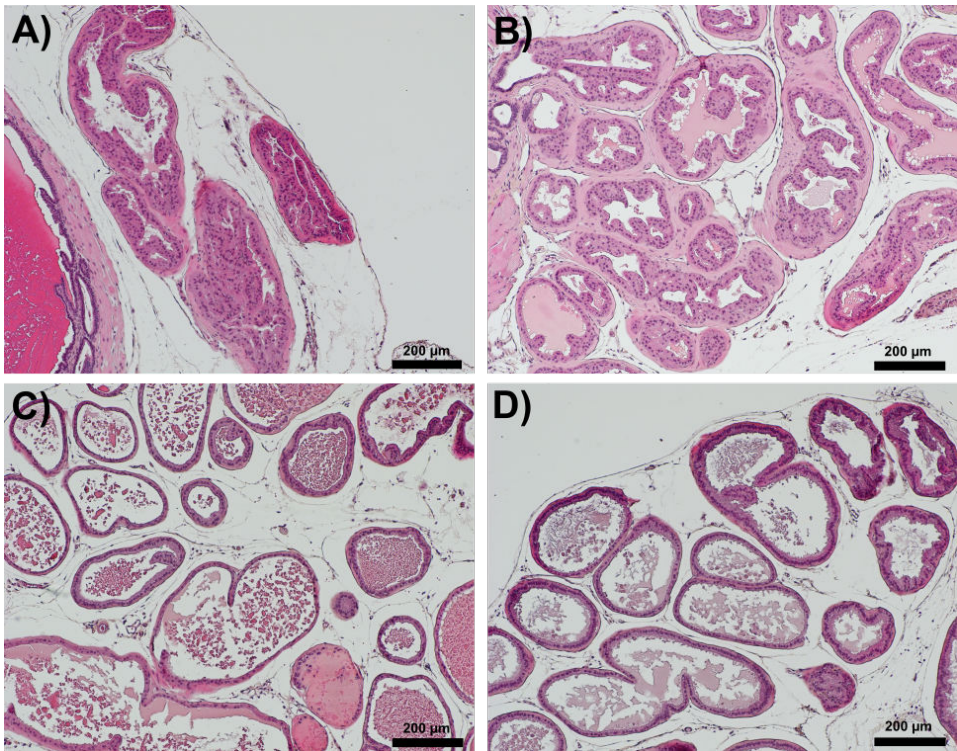
Figure 4.22: Histology images of HES stained tissue sections from the four different lobes of the prostate in a c57 mouse. **A)** shows the AP, **B)** shows the DP, **C)** is the LP and **D)** is the VP.

5 | Discussion

5.1 Interpretation of figures from PCA

In all the loadings plots for PC1 (fig. 4.4 **B)**, 4.11 **B)**, 4.14 **B)**) lipid signals dominate for positive PC1 values, while close to all other metabolites that do not overlap with these lipids are located below zero, which makes PC1 hard to use for anything constructive. It is difficult to deduce anything useful from the lipid signals, because the signals could originate from contamination of the prostate samples with subcutaneous fat that was not completely removed during the microdissection. Looking at the scores plots, the samples seem quite evenly distributed along the PC1 axis, though the PD samples seem to be less spread out. This substantiates the theory of some subcutaneous fat being included in the samples, as avoidance of including fat is easier in relation to tumours because they are more distinct, in addition to some of the samples being taken from the centre of a tumour far from any surrounding fat.

5.1.1 Cancer and non-cancer

The remaining PCs show some clear trends in the data. For PC2 there are some definite clustering of the PD samples below zero (fig. 4.4 **A)**), and while WD and c57 samples are partly overlapping, c57 are definitely higher. Looking at the loadings plot in fig. 4.4 **C)**, this implies that c57 are high in myo-inositol and phosphocholine, PD samples are high in lactate, alanine, taurine and glycine, while the WD samples should have levels of these metabolites that are somewhere between.

For the loadings plot of PC3 (fig. 4.5 **B)**), two metabolites stand out; GPC for positive scores and phosphocholine for negative. In the scores plot in 4.5 **A)**, all PD samples are close to zero, but slightly to the negative side, along the PC3 axis. The WD samples are a bit more spread, while the c57 samples are all spread out from the lowest to the highest along PC3. The content of GPC should therefore be a bit lower than the phosphocholine levels for the PD samples, while the concentrations

of the two metabolites will vary more for both WD and c57 samples. .

Scores on PC4 is also varying within the classifications, but a clear trend is seen with the c57 samples tending to be low on PC4, WD samples are a bit higher, and PD scores are the highest. Citrate is dominating below zero in the loadings plot in **C)**, and will therefore be much higher in c57 than for the other two. Lactate, alanine, creatine, taurine and glycine are important for higher PC4 scores, which mean they are higher in WD and highest in PD.

Fig. 4.6 shows the same trends as have been described, but it reveals that PC2/PC3 clusters PD samples very well, while PC2/PC4 separates all three classes somewhat better. This suggests that the metabolites associated with PC3, in combination with the PC2 metabolites, are more important for finding features that separates PD cancer from both WD and the healthy prostate of c57 mice, while the dominating metabolites in PC4 will help separating all three types nicely, but without a clustering that is as obvious as the one of the tumour samples in the PC2/PC3 combination.

5.1.2   Lobes and tumours

In fig. 4.7 **A)-B)** it becomes evident that the different lobes and tumour samples are quite different. A clear clustering of the tumour samples can be seen at low PC2 scores in **A**, meaning that these samples have the highest levels of the metabolites from the loadings plot (lactate, alanine, taurine, glycine). The other lobes are harder to separate nicely, though there are some clustering of VP samples close to the tumour samples and there is a group of outliers of LP samples. In **B)** the lobes are more separated, with all LP samples below zero on PC3, VP and tumour samples lies close to zero. DP and AP samples varies a bit, but are tending to higher values, in particular the AP samples. Levels of phosphocholine and GPC varies therefore quite a lot for lobes and tumour. Along the PC4 axis, VP samples are low and tumours are high, while the other lobes are located around zero. VP samples are therefore higher in citrate than the others, while tumours are higher in lactate, alanine, creatine, taurine and glycine.

When the samples are labelled with both lobe and c57/TRAMP in the scores plot for PC2/PC4 in fig. 4.9, clustering of samples from same lobe and same mouse model is seen, e.g. the LP samples from c57 that are all high on PC2, and VP samples from c57 which are found at lower PC4 scores than the VP samples from TRAMP.

The PCA of only the c57 samples show much of the same, where LP samples are much higher on PC2 than the others (fig. 4.11), which indicates that they are

high in phosphocholine. PC3 separates VP samples nicely from the others, and the loadings plot in 4.12 **B)** tells that this is due to higher levels of citrate. AP samples tend to be a bit higher on PC3 than the others (high in phosphocholine). In the loadings plot for PC4 in fig. 4.12 **C)**, citrate, taurine and glycine are dominating for positive scores, where close to all VP samples are located along with a mix of other lobes.

For the PCA of the TRAMP samples, fig. 4.14 **A)** too shows some differences between the lobes along the PC2 axis, where tumour samples are lowest, AP samples are the highest, and the other ones lie quite close to each other. Cholines and myo-inositol are high in samples at positive PC2 scores, and lactate, alanine and taurine are in samples at negative scores. The scores plot of PC3/PC4 indicates trends too, with the VP samples low on PC3 scores and tumours are high, with the three other lobes overlapping at around zero. Lactate, alanine, creatine, taurine and glycine are the metabolites which are high for positive PC3 score, and citrate and cholines are high at negative scores. Taurine and glycine are dominating the loadings plot for PC4 (fig. 4.15 **C)**), which seems to separate AP and DP, while the other lobes are varying around zero. The scores plot in fig. 4.16 **A)** shows a nice clustering of both the AP samples, the tumour samples and the VP samples, while the DP and LP samples are more overlapping. Similar trends are seen in fig. 4.16 **B)**.

5.2 Interpretation of figures from peak integration

The bar plots substantiate what the scores plots in chapter 4.2 showed; that there are differences in the metabolites both between non-cancer and the two cancer classifications, and between the different lobes.

5.2.1 Cancer and non-cancer

Fig. 4.17 **A)-B)** shows that lactate, glycine, alanine, taurine and creatine are all positively correlated with PCa, where the highest concentrations are seen in the PD samples. Choline is highest in WD samples, and lowest in c57, but it can still be said to be positively correlated with PCa as it is higher in for both of the two cancer classifications than in c57. GPC, phosphocholine and citrate are all negatively correlated with PCa. This is partly consistent with existing literature(11)(10). Choline has been found to be negatively correlated with PCa in TRAMP compared to c57.

5.2.2   Mouse prostate lobes

The relative concentrations in c57 mice are clearly varying between the different lobes, as fig. 4.18 shows. The concentrations of GPC and phosphocholine are especially striking when looking at **A)**, but looking at fig. **B)**, lactate, citrate and choline have some large variations too. There are also variations in the remaining metabolites (glycine, alanine, taurine and creatine) that is worth noticing, as the percentage differences between the lobes of these metabolites are quite high here as well.

Variations in metabolite concentrations are also seen in TRAMP mice, see fig. 4.19 **A)-E)**. An interesting feature that becomes visible in these plots is that metabolic changes that is seen between c57 and the two cancer classifications all lobes are included in the analysis are not necessarily the same within the four lobes. For example, lactate is expected to be positively correlated with PCa, and that is the case in both DP, LP and VP, but in AP samples it is actually negatively correlated. The same can be seen for GPC, which should be negatively correlated, but in the VP it is the opposite. For citrate, the VP is the only lobe which behaves exactly as expected, while the others do not follow any obvious trends from healthy to the most aggressive cancer (PD). The much higher concentrations of citrate in the VP than in the other lobes can explain why the overall picture gives the impression that citrate is negatively correlated with PCa, while in three of the four lobes that trend is not that clear.

5.2.3   PD tumour

The concentrations of lactate and citrate in PD tumours are higher than in the VP of c57 (fig. 4.20), which are consistent with what was found for the overall picture in fig. 4.17 and previous findings(11).

It has been stated earlier that the choline phospholipid metabolism of PCa in TRAMP mice is altered in a different way than in human disease(11) where the cholines are positively correlated(36)(75), while a decrease of choline levels where found for PCa in TRAMP mice. In fig. 4.20 the concentrations of GPC, phospho-choline and choline are all elevated in PD tumours, in a similar way to human PCa. This suggests that the choline phospholipid metabolism in PD tumours might be different than in WD PCa, and the PD tumours might be a better fit to mimic human PCa with respect to this particular metabolism. In the paper where they conclude with reduced choline concentrations in association with TRAMP PCa, the lobes from each prostate were chosen randomly, and the result of this will the correspond to the results from fig. 4.17, where all lobes are combined.

5.3   Consequences of detected differences

The gross standard deviations in the metabolite concentrations for all $n = 100$ samples in fig. 4.17 can to some extent be explained with the large variations in concentrations within each lobe. For the bar plots where the lobes are separated, however, there are some large standard deviations too. This implies, especially if you look at it in relation to the scores plots from the PCA, that even within a specific lobe there are large variations in metabolite levels. The citrate level in the VP, for instance, may seem to vary a lot based on the standard deviations in both fig. 4.18 **B)** and 4.19 **B)**, and it could therefore be important to be careful not to have too few samples included in further studies to prevent misinterpretations, as the mean levels of the metabolites potentially can be greatly affected by natural fluctuations within lobes. It is worth noting that these variations imply that an increased number of samples n not will reduce the standard deviations, as the standard deviations shown in these plots have their origin in inherent features of the samples, intersample variability and uncertainty in measurement which will be constant regardless of how many samples are included. However, $n = 100$ samples form a sound basis for testing hypotheses with strong statistical power as the standard error in the group mean estimates will be low at this point(76).

The sometimes large variations in metabolite concentrations between the different lobes of the prostate in both healthy c57 mice and in diseased TRAMP mice will clearly effect the results of any studies involving the mouse prostate. E.g. the effect of a PCa treatment which exploits a specific process within the cells might be misinterpreted, as the effect of the treatment on the different lobes could be quite different. It is important to at least be aware of these differences, and it might be necessary to even focus the investigations on one specific lobe, or include all lobes but keep them separate for the analysis of metabolite concentrations.

Since differences in the metabolite levels between the DP and LP have been detected, it could be a mistake to combine these two lobes as the DLP. In the scores plots from the PCA the two lobes are less separated than the other lobes, but some of the plots separates even these two very well, such as in fig. 4.13. In combination with the differences in metabolite concentrations from the peak integration, there is little doubt that one should be careful with treating the DP and the LP as the same with respect to their metabolite contents.

The variations between the lobes of the c57 mice also raises the question of what one should consider as normal or healthy, particularly when one is using absolute quantification. The absolute measure of a metabolite concentration can strongly

depend on in which lobe the measurement is done, and it emphasises the need for controlling which lobe one is analysing.

The differences between the WD PCa and the PD PCa will too have an impact on any results, and the differences should be taken into consideration. The WD and PD PCa might respond and these differences could support the suggestions of sub-types within the TRAMP model(43, 44) where the PD tumours arise in one of the subtypes, while a more slow development from PIN lesions to WD to PD cancer defines another subtype.

5.4   Histology

HES stained tissue sections of the prostates are useful to help explain some of the differences in metabolite levels that were detected on HR-MAS. This analysis will be repeated on histology sections of the actual tissue that HR-MAS was performed on in this thesis, but at the time of writing, the histology has not yet been performed.

The histology images in fig. 4.22 **A)-D)** and 4.21 **A)-E)** show similar features as previous investigations have shown in healthy mouse prostate(14). An obvious difference between the four lobes and the tumour is the luminal space, which there is more of inside the VP than in the other lobes. As citrate is accumulated in the luminal space in human(73), a reason for the higher citrate levels in the VP might be the size of the luminal space. When looking at the image of the tumour in fig 4.21 **E)**, there is very little luminal space, meaning that there is less space left for accumulating citrate. Altered metabolism may, and probably does, still count for some of the differences in citrate concentrations though, and not only the changes in the luminal space(73).

5.5   Comparison to human disease

All metabolites that were identified to be important for detecting differences between cancer and non-cancer in mice in the principal component analysis have been found to play the same role in human disease(36). When investigating all $n = 100$ samples at once, the same trends for which metabolites that are elevated and which are down-regulated in PCa are seen in both human and mice, implying that the metabolic changes are similar. As the different lobes are not always behaving similarly though, it is interesting to see whether any of the lobes mimics human PCa better than the others.

Based on what can be seen in fig. 4.17, the relative concentrations of the metabo-

lites in the VP samples are the only ones that follow the same trends as human PCa for all five metabolites. If it is correctly assumed that the PD tumour samples were from tumours originating in the VP, the relative concentrations in fig. 4.20 adds even more weight to this, as the trends are the same here. The VP may therefore be the lobe that mimics the progression of human PCa best with respect to the metabolic profiles. As the VP is considered to be the only lobe of the mouse prostate without any human counterpart, this suggestion is surprising, but in consequence all the more important.

5.6   Further perspectives

An important step forward would be to perform histopathology on all TRAMP samples that were used for the HR-MAS MRS, especially on the ones that were classified as WD, to confirm if there actually is cancer there and if the classifications are suitable. With this knowledge one can be even more certain about the differences between the WD and PD cancers in TRAMP prostate.

As changes in the polyamines are associated with PCa, and therefore suggested as a biomarker for the disease(26, 77, 78), investigation into these metabolites in relationship to the c57 and TRAMP prostates will be interesting. To do so, the NOESY spectra will have to be analysed, as the polyamines are not visible in the CPMG spectra. Involving more metabolites in the integration for the different lobes and PD tumour will also be interesting in order to improve the comparison both between the lobes and between the cancer classifications.

Concentrations of metabolites are often treated in terms of ratios, such as the citrate to creatine peak(10), the GPC to phosphocholine peak(79), or the choline to creatine peak(80). Similar calculations would therefore faciliate comparison of findings within the lobes with what is found in human disease.

Absolute quantification of the spectra could be performed to improve the comparison to human PCa, as absolute concentrations for the progression of the disease in humans are known(36). Absolute concentrations could also be used to investigate more closely which lobe of the mouse prostate that are more similar to the human prostate, as the levels in the TRAMP mice might even be in a completely different order in some or all of the lobes. For absolute quantification, the NOESY spectra will have to be used, as the CPMG spectra are T2 filtered, which affects the peak areas. The same HR-MAS MRS procedure as was performed during this project will then be applied to a reference sample with known content of a certain metabolite, which then can be used to quantify the spectra.

As the PQN and Pareto scaling are among the most widely used normalisation

methods in preprocessing of MRS data, these methods were used in this project as well. Investigations into the effect of different methods have though been performed, where Quantile Normalisation(81, 82) and Histogram Matching(62) have outperformed other commonly used methods. For the absolute quantification of the metabolites one of these methods should therefore be applied instead.

6 | Conclusion

The overall trends for the PCa progression in mice are similar to what is found in human disease, where metabolic changes are detected in relation to both energy and phospholipid metabolism. Lactate, alanine, creatine, glycine and taurine are all positively correlated with the disease in both human and mice, and citrate, GPC, phosphocholine and choline are negatively correlated. This implies that TRAMP cancer is metabolically similar to human PCa, which suggests that the model can provide clinically relevant information from studies that investigate metabolic changes in prostate cancer, such as therapeutic effects.

Trends caused by the same metabolites as mentioned above are causing clustering in the data also within the different lobes of the mouse prostate. Peak integration revealed that the metabolite concentrations varies greatly between the four different lobes of the mouse prostate, both for the c57 and the TRAMP mice. Special care should therefore be taken when measuring metabolic changes in response to e.g. treatments of PCa, as the differences in concentrations of metabolites may lead to misinterpretation of the results. The differences between the DP and LP in metabolite concentrations also imply that one should be careful with treating these two lobes as the same, which have been common practice based on their similarities in histology. Surprisingly, the VP seems to be the prostate lobe that mimics the progression of PCa in humans best, despite being considered not to have a human counterpart based on histology.

Histology images reveals that the luminal spaces the four lobes of the prostate in TRAMP mice are similar to those of c57 mice, and the large differences in citrate concentrations may partly be due to this.

Performing histopathology on the TRAMP samples that were used in this project would be an useful addition to this project to validate the presence, and extent, of cancer in all TRAMP samples, and to confirm if the classifications are suitable.

Using the NOESY spectra instead of the CPMG spectra, absolute quantification and metabolite peak ratios can be calculated in order to improve comparison to

human disease. Including more metabolites, such as the polyamines, is also of great interest, as these are considered possible biomarkers of PCa. Applying the Quantile Normalisation instead of other widely used methods will also improve the analysis, as it has been proven to outperform other methods.

In summary, this work has uncovered some important considerations when using mouse models of prostate cancer. While the TRAMP cancer shows metabolic similarities to human PCa, there is also significant variation in the metabolic profiles of different prostate lobes, both in TRAMP and healthy (c57) mice. The different metabolic profiles of mouse prostate lobes have great implications for future studies that utilise mouse models of PCa, as the results of this thesis show that without careful tissue selection, natural variations in metabolite levels between lobes may be misleading when interpreting results.

References

[1] Lindsey A Torre, Freddie Bray, Rebecca L Siegel, Jacques Ferlay, Joannie Lortet-Tieulent, and Ahmedin Jemal. Global cancer statistics, 2012. *CA: a cancer journal for clinicians*, 65(2):87–108, 2015.

[2] Thomas A Stamey, Norman Yang, Alan R Hay, John E McNeal, Fuad S Freiha, and Elise Redwine. Prostate-specific antigen as a serum marker for adenocarcinoma of the prostate. *New England Journal of Medicine*, 317(15):909–916, 1987.

[3] Joseph E Oesterling. Prostate specific antigen: a critical assessment of the most useful tumor marker for adenocarcinoma of the prostate. *The Journal of urology*, 145(5):907–923, 1991.

[4] Gerrit Draisma, Rob Boer, Suzie J Otto, Ingrid W van der Cruijsen, Ronald AM Damhuis, Fritz H Schroder, and Harry J de Koning. Lead times and overdetection due to prostate-specific antigen screening: estimates from the european randomized study of screening for prostate cancer. *Journal of the National Cancer Institute*, 95(12):868–878, 2003.

[5] Joanna B Madalinska, Marie-Louise Essink-Bot, Harry J de Koning, Wim J Kirkels, Paul J van der Maas, and Fritz H Schroder. Health-related quality-of-life effects of radical prostatectomy and primary radiotherapy for screen-detected or clinically diagnosed localized prostate cancer. *Journal of Clinical Oncology*, 19(6):1619–1628, 2001.

[6] Patrick A Everley, Jeroen Krijgsveld, Bruce R Zetter, and Steven P Gygi. Quantitative cancer proteomics: stable isotope labeling with amino acids in cell culture (silac) as a tool for prostate cancer research. *Molecular & Cellular Proteomics*, 3(7):729–735, 2004.

[7] Robert A Stephenson, Colin PN Dinney, Kazuo Gohji, Nelson G Ordonez, Jerald J Killion, and Isaiah J Fidler. Metastatic model for human prostate

cancer using orthotopic implantation in nude mice. *Journal of the National Cancer Institute*, 84(12):951–957, 1992.

[8] Michael Ittmann, Jiaoti Huang, Enrico Radaelli, Philip Martin, Sabina Signoretti, Ruth Sullivan, Brian W Simons, Jerrold M Ward, Brian D Robinson, Gerald C Chu, et al. Animal models of human prostate cancer: the consensus report of the new york meeting of the mouse models of human cancers consortium prostate pathology committee. *Cancer research*, 73(9):2718–2736, 2013.

[9] Magdalena M Grabowska, David J DeGraff, Xiuping Yu, Ren Jie Jin, Zhenbang Chen, Alexander D Borowsky, and Robert J Matusik. Mouse models of prostate cancer: picking the best model for the question. *Cancer and Metastasis Reviews*, 33:377–397, 2014.

[10] Leslie C Costello, Renty B Franklin, Jing Zou, Pei Feng, Robert Bok, Mark G Swanson, and John Kurhanewicz. Human prostate cancer zip1/zinc/citrate genetic/metabolic relationship in the tramp prostate cancer animal model. *Cancer biology & therapy*, 12(12):1078–1084, 2011.

[11] Friederike Teichert, Richard D Verschoyle, Peter Greaves, Richard E Edwards, Orla Teahan, Donald JL Jones, Ian D Wilson, Peter B Farmer, William P Steward, Timothy W Gant, et al. Metabolic profiling of transgenic adenocarcinoma of mouse prostate (tramp) tissue by 1h-nmr analysis: evidence for unusual phospholipid metabolism. *The Prostate*, 68(10):1035–1047, 2008.

[12] Silje Løveng. Metabolic profiling of prostate cancer tissue using magnetic resonance spectroscopy - A comparison between human and mouse prostate cancer, 2017. Unpublished project thesis, NTNU.

[13] John E McNeal. Regional morphology and pathology of the prostate. *American journal of clinical pathology*, 49(3):347–357, 1968.

[14] Daniel SM Oliveira, Sijana Dzinic, Alan I Bonfil, Allen D Saliganan, Shijie Sheng, and R Daniel Bonfil. The mouse prostate: a basic anatomical and histological guideline. *Bosnian Journal of Basic Medical Sciences*, 16(1):8, 2016.

[15] Isabelle M Berquin, Younong Min, Ruping Wu, Hong Wu, and Yong Q Chen. Expression signature of the mouse prostate. *Journal of Biological Chemistry*, 280(43):36442–36451, 2005.

[16] Cory Abate-Shen and Michael M Shen. Molecular genetics of prostate cancer. *Genes & development*, 14(19):2410–2434, 2000.

[17] Douglas Hanahan and Robert A Weinberg. Hallmarks of cancer: the next generation. *cell*, 144(5):646–674, 2011.

[18] Douglas Hanahan and Robert A Weinberg. The hallmarks of cancer. *cell*, 100(1):57–70, 2000.

[19] Jeff Hardin, Gregory Paul Bertoni, and Lewis J Kleinsmith. *Becker's World of the Cell*. Pearson Education, Inc., 2012.

[20] Nasjonalt kvalitetsregister for prostatakreft. *Årsrapport for prostatakreft 2015*. Kreftregisteret, 2016.

[21] John E McNeal, Elise A Redwine, Fuad S Freiha, and Thomas A Stamey. Zonal distribution of prostatic adenocarcinoma: correlation with histologic pattern and direction of spread. *The American journal of surgical pathology*, 12(12):897–906, 1988.

[22] Masanori Noguchi, Thomas A Stamey, JOHN E Mc NEAL, and Cheryl EM Yemoto. An analysis of 148 consecutive transition zone cancers: clinical and histological characteristics. *The Journal of urology*, 163(6):1751–1755, 2000.

[23] Sébastien Bouyé, Eric Potiron, Philippe Puech, Xavier Leroy, Laurent Lemaitre, and Arnauld Villers. Transition zone and anterior stromal prostate cancers: zone of origin and intraprostatic patterns of spread at histopathology. *The Prostate*, 69(1):105–113, 2009.

[24] David G Bostwick. Prostatic intraepithelial neoplasia. *Current urology reports*, 1(1):65–70, 2000.

[25] Lukas Bubendorf, Alain Schöpfer, Urs Wagner, Guido Sauter, Holger Moch, Niels Willi, Thomas C Gasser, and Michael J Mihatsch. Metastatic patterns of prostate cancer: an autopsy study of 1,589 patients. *Human pathology*, 31(5):578–583, 2000.

[26] Guro F Giskeødegård, Helena Bertilsson, Kirsten M Selnæs, Alan J Wright, Tone F Bathen, Trond Viset, Jostein Halgunset, Anders Angelsen, Ingrid S Gribbestad, and May-Britt Tessem. Spermine and citrate as metabolic biomarkers for assessing prostate cancer aggressiveness. *PloS one*, 8(4):e62375, 2013.

[27] May-Britt Tessem, Mark G Swanson, Kayvan R Keshari, Mark J Albers, David Joun, Z Laura Tabatabai, Jeffry P Simko, Katsuto Shinohara, Sarah J Nelson, Daniel B Vigneron, et al. Evaluation of lactate and alanine as metabolic biomarkers of prostate cancer using 1h hr-mas spectroscopy of biopsy tissues. *Magnetic resonance in medicine*, 60(3):510–516, 2008.

[28] Saravana M Dhanasekaran, Terrence R Barrette, Debashis Ghosh, Rajal Shah, Sooryanarayana Varambally, Kotoku Kurachi, Kenneth J Pienta, Mark A Rubin, and Arul M Chinnaiyan. Delineation of prognostic biomarkers in prostate cancer. *Nature*, 412(6849):822–826, 2001.

[29] Michael T Madigan, John M Martinko, Kelly S Bender, Daniel H Buckley, and David A Stahl. *Brock biology of microorganisms 14th ed.* Pearson Education Limited, 2015.

[30] Eugene P Kennedy and Samuel B Weiss. The function of cytidine coenzymes in the biosynthesis of phospholipids. *Journal of Biological Chemistry*, 222(1):193–214, 1956.

[31] JP Kavanagh. Sodium, potassium, calcium, magnesium, zinc, citrate and chloride content of human prostatic and seminal fluid. *Journal of reproduction and fertility*, 75(1):35–41, 1985.

[32] Leslie C Costello and Renty B Franklin. The clinical relevance of the metabolism of prostate cancer; zinc and tumor suppression: connecting the dots. *Molecular cancer*, 5(1):17, 2006.

[33] John Kurhanewicz, Daniel B Vigneron, Sarah J Nelson, Hedvig Hricak, Jeffrey M MacDonald, Badrinath Konety, and Perinchery Narayan. Citrate as an in vivo marker to discriminate prostate cancer from benign prostatic hyperplasia and normal prostate peripheral zone: detection via localized proton spectroscopy. *Urology*, 45(3):459–466, 1995.

[34] Sebastian A Müller, Korbinian Holzapfel, Christof Seidl, Uwe Treiber, Bernd J Krause, and Reingard Senekowitsch-Schmidtke. Characterization of choline uptake in prostate cancer cells following bicalutamide and docetaxel treatment. *European journal of nuclear medicine and molecular imaging*, 36(9):1434–1442, 2009.

[35] Mark G Swanson, Kayvan R Keshari, Z Laura Tabatabai, Jeffry P Simko, Katsuto Shinohara, Peter R Carroll, Andrew S Zektzer, and John Kurhanewicz. Quantification of choline-and ethanolamine-containing metabolites in human prostate tissues using 1h hr-mas total correlation spectroscopy. *Magnetic resonance in medicine*, 60(1):33–40, 2008.

[36] Elise Sandsmark. Metabolic alterations associated with proliferation and progression of human prostate cancer, student thesis in medicine. 2015.

[37] Matthew G Vander Heiden, Lewis C Cantley, and Craig B Thompson. Understanding the warburg effect: the metabolic requirements of cell proliferation. *science*, 324(5930):1029–1033, 2009.

[38] Mark J Albers, Robert Bok, Albert P Chen, Charles H Cunningham, Matt L Zierhut, Vickie Yi Zhang, Susan J Kohler, James Tropp, Ralph E Hurd, Yi-Fen Yen, et al. Hyperpolarized 13c lactate, pyruvate, and alanine: noninvasive biomarkers for prostate cancer detection and grading. *Cancer research*, 68(20):8607–8615, 2008.

[39] Takahiko Suwa, Abraham Nyska, Joseph K Haseman, Joel F Mahler, and Robert R Maronpot. Spontaneous lesions in control b6c3f1 mice and recommended sectioning of male accessory sex organs. *Toxicologic pathology*, 30(2):228–234, 2002.

[40] JR Gingrich and NM Greenberg. A transgenic mouse prostate cancer model. *Toxicologic pathology*, 24(4):502–504, 1996.

[41] Arthur A Hurwitz, Barbara A Foster, James P Allison, Norman M Greenberg, and Eugene D Kwon. The tramp mouse as a model for prostate cancer. *Current protocols in immunology*, pages 20–5, 2001.

[42] Jeffrey R Gingrich, Roberto J Barrios, Ronald A Morton, Brendan F Boyce, Francesco J DeMayo, Milton J Finegold, Roxani Angelopoulou, Jeffrey M Rosen, and Norman M Greenberg. Metastatic prostate cancer in a transgenic mouse. *Cancer research*, 56(18):4096–4102, 1996.

[43] Deborah K Hill, Eugene Kim, Jose R Teruel, Yann Jamin, Marius Widerøe, Caroline D Søgaard, Øystein Størkersen, Daniel N Rodrigues, Andreas Heindl, Yinyin Yuan, et al. Diffusion-weighted mri for early detection and characterization of prostate cancer in the transgenic adenocarcinoma of the mouse prostate model. *Journal of Magnetic Resonance Imaging*, 43(5):1207–1217, 2016.

[44] Teresa Chiaverotti, Suzana S Couto, Annemarie Donjacour, Jian-Hua Mao, Hiroki Nagase, Robert D Cardiff, Gerald R Cunha, and Allan Balmain. Dissociation of epithelial and neuroendocrine carcinoma lineages in the transgenic adenocarcinoma of mouse prostate model of prostate cancer. *The American journal of pathology*, 172(1):236–246, 2008.

[45] Felix Bloch. Nuclear induction. *Physical review*, 70(7-8):460, 1946.

[46] Edward M Purcell, HC Torrey, and Robert V Pound. Resonance absorption by nuclear magnetic moments in a solid. *Physical review*, 69(1-2):37, 1946.

[47] Joseph P Cousins. Clinical mr spectroscopy: fundamentals, current applications, and future potential. *AJR. American journal of roentgenology*, 164(6):1337–1347, 1995.

[48] Per Chr Hemmer. *Kvantemekanikk*. Tapir, 1985.

[49] Pieter Zeeman. The effect of magnetisation on the nature of light emitted by a substance. *Nature*, 55(1424):347, 1897.

[50] ER Andrew, A Bradbury, and RG Eades. Nuclear magnetic resonance spectra from a crystal rotated at high speed. 1958.

[51] Frank AL Anet and AJR Bourn. Nuclear magnetic resonance spectral assignments from nuclear overhauser effects1. *Journal of the American Chemical Society*, 87(22):5250–5251, 1965.

[52] WA Anderson and R Freeman. Influence of a second radiofrequency field on high-resolution nuclear magnetic resonance spectra. *The Journal of Chemical Physics*, 37(1):85–103, 1962.

[53] Ryan T Mckay. How the 1d-noesy suppresses solvent signal in metabonomics nmr spectroscopy: An examination of the pulse sequence components and evolution. *Concepts in Magnetic Resonance Part A*, 38(5):197–220, 2011.

[54] Lawrence P. McIntosh. *CPMG*, pages 386–386. Springer Berlin Heidelberg, Berlin, Heidelberg, 2013.

[55] WP Aue, J Karhan, and RR Ernst. Homonuclear broad band decoupling and two-dimensional j-resolved nmr spectroscopy. *The Journal of Chemical Physics*, 64(10):4226–4227, 1976.

[56] Christian Ludwig and Mark R Viant. Two-dimensional j-resolved nmr spectroscopy: review of a key methodology in the metabolomics toolbox. *Phytochemical Analysis*, 21(1):22–32, 2010.

[57] Frans A. A. Mulder and Ruud M. Scheek. *Multidimensional NMR Spectroscopy*, pages 1637–1646. Springer Berlin Heidelberg, Berlin, Heidelberg, 2013.

[58] Paul HC Eilers. A perfect smoother. *Analytical chemistry*, 75(14):3631–3636, 2003.

[59] Paul HC Eilers and Hans FM Boelens. Baseline correction with asymmetric least squares smoothing. *Leiden University Medical Centre Report*, 1:1, 2005.

[60] Leslie R Euceda, Guro F Giskeødegård, and Tone F Bathen. Preprocessing of nmr metabolomics data. *Scandinavian journal of clinical and laboratory investigation*, 75(3):193–203, 2015.

[61] Frank Dieterle, Alfred Ross, Götz Schlotterbeck, and Hans Senn. Probabilistic quotient normalization as robust method to account for dilution of complex biological mixtures. application in 1h nmr metabonomics. *Analytical chemistry*, 78(13):4281–4290, 2006.

[62] RJO Torgrip, KM Åberg, E Alm, I Schuppe-Koistinen, and J Lindberg. A note on normalization of biofluid 1d 1h-nmr data. *Metabolomics*, 4(2):114–121, 2008.

[63] Andrew Craig, Olivier Cloarec, Elaine Holmes, Jeremy K Nicholson, and John C Lindon. Scaling and normalization effects in nmr spectroscopic metabonomic data sets. *Analytical chemistry*, 78(7):2262–2267, 2006.

[64] Lennart Eriksson, Henrik Antti, Johan Gottfries, Elaine Holmes, Erik Johansson, Fredrik Lindgren, Ingrid Long, Torbjörn Lundstedt, Johan Trygg, and Svante Wold. Using chemometrics for navigating in the large data sets of genomics, proteomics, and metabonomics (gpm). *Analytical and bioanalytical chemistry*, 380(3):419–429, 2004.

[65] Bradley Worley and Robert Powers. Multivariate analysis in metabolomics. *Current Metabolomics*, 1(1):92–107, 2013.

[66] Karl Pearson. Liii. on lines and planes of closest fit to systems of points in space. *The London, Edinburgh, and Dublin Philosophical Magazine and Journal of Science*, 2(11):559–572, 1901.

[67] Harold Hotelling. Analysis of a complex of statistical variables into principal components. *Journal of educational psychology*, 24(6):417, 1933.

[68] Tonje H Haukaas, Leslie R Euceda, Guro F Giskeødegård, Santosh Lamichhane, Marit Krohn, Sandra Jernström, Miriam R Aure, Ole C Lingjærde, Ellen Schlichting, Øystein Garred, et al. Metabolic clusters of breast cancer in relation to gene-and protein expression subtypes. *Cancer & Metabolism*, 4(1):12, 2016.

[69] Francesco Savorani, Giorgio Tomasi, and Søren Balling Engelsen. icoshift: A versatile tool for the rapid alignment of 1d nmr spectra. *Journal of Magnetic Resonance*, 202(2):190–202, 2010.

[70] Human metabolome database. `http://www.hmdb.ca/`.

[71] Robert A van den Berg, Huub CJ Hoefsloot, Johan A Westerhuis, Age K Smilde, and Mariët J van der Werf. Centering, scaling, and transformations: improving the biological information content of metabolomics data. *BMC genomics*, 7(1):142, 2006.

[72] Rasmus Bro and Age K Smilde. Centering and scaling in component analysis. *Journal of Chemometrics*, 17(1):16–33, 2003.

[73] György Kovács and Peter Hoskin. *Interstitial Prostate Brachytherapy: LDR-PDR-HDR*. Springer Science & Business Media, 2013.

[74] Jinhui Zhang, Lei Wang, Yong Zhang, Li Li, Suni Tang, Chengguo Xing, Sung-Hoon Kim, Cheng Jiang, and Junxuan Lü. Chemopreventive effect of korean angelica root extract on tramp carcinogenesis and integrative "omic" profiling of affected neuroendocrine carcinomas. *Molecular carcinogenesis*, 54(12):1567–1583, 2015.

[75] John Kurhanewicz, Daniel B Vigneron, and Sarah J Nelson. Three-dimensional magnetic resonance spectroscopic imaging of brain and prostate cancer. *Neoplasia*, 2(1-2):166–189, 2000.

[76] Deirdre N McCloskey and Stephen T Ziliak. The standard error of regressions. *Journal of economic literature*, 34(1):97–114, 1996.

[77] Natalie J Serkova, Eduard J Gamito, Richard H Jones, Colin O'donnell, Jaimi L Brown, Spencer Green, Holly Sullivan, Tammy Hedlund, and E David Crawford. The metabolites citrate, myo-inositol, and spermine are potential age-independent markers of prostate cancer in human expressed prostatic secretions. *The Prostate*, 68(6):620–628, 2008.

[78] Marinette van der Graaf, Raymond G Schipper, Gosse ON Oosterhof, Jack A Schalken, Albert AJ Verhofstad, and Arend Heerschap. Proton mr spectroscopy of prostatic tissue focused on the etection of spermine, a possible biomarker of malignant behavior in prostate cancer. *Magnetic Resonance Materials in Physics, Biology and Medicine*, 10(3):153–159, 2000.

[79] Ellen Ackerstaff, Kristine Glunde, and Zaver M Bhujwalla. Choline phospholipid metabolism: a target in cancer cells? *Journal of cellular biochemistry*, 90(3):525–533, 2003.

[80] Tone F Bathen, Beathe Sitter, Torill E Sjøbakk, May-Britt Tessem, and Ingrid S Gribbestad. Magnetic resonance metabolomics of intact tissue: a biotechnological tool in cancer diagnostics and treatment evaluation. *Cancer research*, 70(17):6692–6696, 2010.

[81] Benjamin M Bolstad, Rafael A Irizarry, Magnus Åstrand, and Terence P Speed. A comparison of normalization methods for high density oligonucleotide array data based on variance and bias. *Bioinformatics*, 19(2):185–193, 2003.

[82] Stefanie M Kohl, Matthias S Klein, Jochen Hochrein, Peter J Oefner, Rainer Spang, and Wolfram Gronwald. State-of-the art data normalization methods improve nmr-based metabolomic analysis. *Metabolomics*, 8(1):146–160, 2012.

Appendices

A | Lab sheet for HR-MAS MRS experiments

Figure A.1: The layout of the sheet that was used to make notes during sample preparation and HR-MAS MRS.

B | Sample information and parameters for the HR-MAS MRS

The following table details sample information for the HR-MAS MRS experiments.

Table B.1: Sample information and corresponding parameters for the HR-MAS MRS experiments. For each sample, the age at which the mouse were terminated, the weight of the tissue and the weight of the D_2O solution is noted. $O1$ is the water suppression pulse, $P1$ is the $90°$ pulse, and the shim is measured by the Full Width at Half Maximum (FWHM) of the formate peak.

Sample	Age (weeks)	Weight (mg)	D_2O (mg)	$O1$ (μs)	$P1$ (μs)	Shim (Hz)
326 (1) tumour	26.7	10.9	3.3	2815.40	13.55	1.00
350 LP (2)	22.7	13.5	3.4	2815.50	13.63	1.05
350 VP	22.7	10.8	3.3	2815.20	14.00	1.30
538 DP	48.9	9.2	3.4	2814.80	13.63	1.07
538 VP	48.9	7.1	3.3	2816.80	13.50	0.70
543 (1)	28.9	8.9	3.4	2815.65	13.38	1.30
543 (2)	28.9	7.3	3.5	2816.00	13.43	1.47
544 VP	28.9	7.8	2.5	2813.00	13.75	1.50
554 (2) rim	22.9	9.0	3.3	2815.45	14.06	1.20
554 (3) centre	22.9	10.2	3.5	2814.90	13.73	1.40
562 AP	41.2	9.5	7.2	2817.00	10.03	0.78
562 DP	41.2	11.3	5.9	2817.00	10.23	0.47
562 LP1	41.2	9.6	8.5	2817.44	10.10	1.50
562 LP2 tumour	41.2	8.1	6.7	2817.44	10.11	0.78
562 VP	41.2	8.3	8.2	2017.35	10.08	1.50
568 AP	39.6	9.0	7.4	2817.35	10.03	0.90
568 DP brown	39.6	7.6	6.0	2818.00	9.96	1.07
568 LP	39.6	6.6	13.9	2819.00	9.93	2.15
568 VP	39.6	7.8	5.9	2818.20	9.93	1.62
569 DP1	39.6	7.6	5.8	2817.80	10.15	0.70
569 DP2	39.6	8.6	5.6	2815.30	10.08	0.92

Sample	Age (weeks)	Weight (mg)	D_2O (mg)	$O1$ (μs)	$P1$ (μs)	Shim (Hz)
569 LP1 rim	39.6	8.9	6.9	2817.20	9.98	0.52
569 LP2 centre	39.6	8.2	6.1	2817.20	10.13	2.20
569 VP	39.6	5.6	6.8	2816.00	10.00	1.47
570 AP	39.6	11.1	6.8	2816.80	10.20	0.60
570 DP	39.6	14.6	6.4	2817.05	10.23	0.60
570 DP tumour	39.6	9.7	7.9	2817.00	10.19	0.56
570 LP	39.6	6.3	5.9	2816.95	10.03	1.40
570 VP	39.6	10.4	6.0	2817.13	10.15	0.66
577 AP	20.4	19.4	3.3	2816.70	13.40	1.60
577 DP	20.4	9.2	3.4	2815.19	13.53	1.15
577 LP	20.4	5.4	3.1	2815.40	13.48	1.34
577 VP	20.4	10.4	3.3	2814.00	13.58	1.56
580 AP	27.86	6.8	10.9	2819.40	10.08	0.75
580 DP	27.86	9.5	4.2	2816.80	10.00	0.61
580 LP	27.86	9.4	3.0	2817.00	10.06	1.30
580 VP	27.86	8.6	3.0	2818.50	9.88	1.54
581 AP	27.86	9.1	3.7	2815.00	10.06	1.04
581 AP2	27.86	7.6	6.0	2810.00	12.38	0.90
581 DP	27.86	10.9	5.9	2820.00	11.38	1.50
581 DP2	27.86	8.1	6.0	2817.80	9.95	0.60
581 LP	27.86	7.7	3.0	2816.00	10.03	0.90
581 VP	27.86	10.4	3.0	2818.00	10.13	1.40
582 AP	27.86	12.7	6.0	2819.00	9.95	1.64
582 DP	27.86	8.8	7.3	2820.00	9.95	1.90

Sample	Age (weeks)	Weight (mg)	D_2O (mg)	$O1$ (μs)	$P1$ (μs)	Shim (Hz)
582 LP	27.86	6.0	6.1	2817.40	10.06	0.58
582 VP	27.86	12.2	6.0	2817.20	10.03	0.56
588 AP	29.14	8.3	7.3	2816.90	10.07	0.52
588 DP	29.14	11.5	6.3	2816.80	10.07	0.49
588 DP tumour	29.14	10.1	7.1	2816.89	10.26	0.57
588 LP	29.14	12.5	7.8	2816.60	10.20	0.50
588 VP	29.14	12.4	7.6	2816.50	10.18	0.55
589 AP	29.14	7.4	6.4	2816.60	10.00	1.60
589 DP	29.14	8.6	5.4	2815.00	10.09	0.47
589 PD3	29.14	9.2	8.0	2817.36	10.19	0.70
589 tumour centre	29.14	11.8	7.2	2817.00	10.15	0.95
589 tumour rim 1	29.14	11.8	8.8	2816.90	10.02	1.20
589 tumour rim 2	29.14	10.3	7.3	2816.70	10.13	0.45
589 VP	29.14	8.0	8.0	2817.48	10.15	1.00
591 AP	30	13.8	5.7	2817.20	10.05	0.74
591 DP	30	8.9	8.3	2815.30	10.00	1.28
591 LP	30	8.2	8.2	2817.00	10.08	0.48
591 VP	30	9.5	8.4	2017.03	10.13	0.89
c57-7 AP	31.86	8.4	7.3	2817.38	10.08	0.83
c57-7 DP	31.86	8.8	8.1	2817.40	10.13	1.05
c57-7 LP	31.86	8.2	7.0	2816.10	10.09	1.30
c57-7 VP	31.86	13.0	7.1	2817.30	10.35	0.85
c57-8 AP	31.86	11.6	6.1	2817.50	10.03	1.90
c57-8 DP	31.86	9.8	5.9	2816.80	10.03	1.20

Sample	Age (weeks)	Weight (mg)	D_2O (mg)	$O1$ (μs)	$P1$ (μs)	Shim (Hz)
c57-8 LP	31.86	7.9	8.0	2817.50	10.05	1.50
c57-8 VP	31.86	7.4	8.5	2816.80	10.05	1.50
c57-9 AP	27.86	7.5	6.6	2819.00	10.18	2.60
c57-9 DP	27.86	8.1	10.7	2818.00	10.23	1.15
c57-9 LP	27.86	4.5	10.5	2818.00	10.10	1.90
c57-9 VP	27.86	9.8	7.4	2816.30	10.03	1.30
c57-10 AP	27.86	11.0	7.1	2826.00	10.03	1.90
c57-10 DP	27.86	7.3	7.4	2815.80	10.05	2.15
c57-10 LP	27.86	6.0	6.5	2816.50	10.25	2.40
c57-10 VP	27.86	6.7	7.0	2816.50	10.10	1.15
c57-11 AP	27.86	6.5	6.0	2815.90	10.13	1.60
c57-11 DP	29.86	8.8	7.7	2819.00	10.25	1.30
c57-11 LP	29.86	8.0	8.1	2815.40	10.05	0.90
c57-11 VP	29.86	7.8	7.8	2818.00	10.06	0.69
c57-12 AP	29.86	8.9	5.5	2814.90	10.13	0.76
c57-12 DP	29.86	12.4	7.2	2814.60	10.15	1.15
c57-12 LP	29.86	7.0	6.9	2827.90	9.98	0.65
c57-12 VP	29.86	9.6	7.5	2815.00	10.25	0.37
c57-13 AP	29.86	11.5	8.7	2814.80	10.03	1.38
c57-13 DP	29.86	7.9	8.0	2817.00	10.31	1.41
c57-13 LP	29.86	5.9	6.9	2815.50	10.05	1.15
c57-13 VP	29.86	5.5	8.1	2817.00	10.07	1.43
c57-13 VP2	29.86	4.0	6.8	2816.00	10.00	0.70
c57-14 AP	39.14	8.8	6.6	2817.32	9.97	0.90

Sample	Age (weeks)	Weight (mg)	D_2O (mg)	$O1$ (μs)	$P1$ (μs)	Shim (Hz)
c57-14 DP	39.14	7.8	7.7	2818.55	10.13	1.12
c57-14 LP	39.14	5.2	8.6	2818.00	10.28	1.00
c57-14 VP	39.14	8.3	7.8	2816.63	10.23	1.47
c57-15 AP	40.29	13.3	8.0	2817.00	10.02	1.30
c57-15 DP	40.29	8.1	8.7	2816.80	10.04	1.60
c57-15 LP	40.29	11.5	5.9	2817.00	10.05	1.70
c57-15 VP	40.29	10.3	6.2	2816.63	9.95	0.60